CIVIL ENGINEERING STUDIES

STRUCTURAL RESEARCH SERIES NO. 363

LUMPED-PARAMETER ANALYSIS FOR SHEAR FAILURE IN THE END SLAB OF CYLINDRICAL PRESTRESSED CONCRETE PRESSURE VESSELS

By

R. Higashionna

and

W. C. Schnobrich

Subcontract No. 2906
Under Contract No. W-7405-eng-26

A REPORT ON AN INVESTIGATION
CARRIED OUT AS PART OF THE
PRESTRESSED CONCRETE REACTOR VESSEL PROGRAM
OF THE
OAK RIDGE NATIONAL LABORATORY

Operated by
Union Carbide Corporation
for the
U. S. Atomic Energy Commission

UNIVERSITY OF ILLINOIS

URBANA, ILLINOIS

AUGUST, 1970

LUMPED-PARAMETER ANALYSIS FOR SHEAR FAILURE IN THE END SLAB OF CYLINDRICAL PRESTRESSED CONCRETE PRESSURE VESSELS

By

R. Higashionna
and
W. C. Schnobrich

AUGUST 1970

Subcontract No. 2906
Under Contract No. W-7405-eng-26

A Report on an Investigation
carried out as part of the
Prestressed Concrete Reactor Vessel Program
of the
Oak Ridge National Laboratory

Operated by
Union Carbide Corporation
for the
U. S. Atomic Energy Commission

University of Illinois
Urbana, Illinois

ACKNOWLEDGMENT

The study presented in this report was carried out as a part of the Prestressed Concrete Reactor Vessel Program of the Oak Ridge National Laboratory, sponsored by the United States Atomic Energy Commission. The program is coordinated by G. D. Whitman of the Oak Ridge National Laboratory.

Acknowledgment is due B. Mohraz, Assistant Professor of Civil Engineering, for his assistance in the development of the computer program and B. I. Karlsson, Research Assistant in Civil Engineering for providing the data for the experimental checks.

TABLE OF CONTENTS

Page

LIST OF FIGURES

FIGURE Page

1. INTRODUCTION

1.1 Background Information

To house a gas-cooled nuclear reactor which requires a large core space the use of prestressed concrete reactor vessels (PCRV's) has been adopted. The shapes for prestressed concrete reactor vessels have varied from a cylinder bounded by two inverted hemispherical heads to a spherical shell. The present trend in the design of PCRV's is towards cylindrical barrels capped with flat, end slabs.

The PCRV's with flat, end slabs may fail in one or more of the four major failure modes: a longitudinal cracking in the wall, a circumferential cracking in the wall, a flexural failure in the end slab, and a shear failure in the end slab. The wall failures are well defined and can be prevented by using adequate circumferential and longitudinal prestressing. The design of end slabs has been hampered by a lack of sufficient understanding of the end slab failure mechanism. Several investigators have studied the complex end slab behavior in the hope of obtaining a better understanding of the failure modes.

A series of tests on small-scale cylindrical prestressed concrete reactor vessels has been conducted at the Structural Research Laboratory of the University of Illinois Department of Civil Engineering (1, 2). Figure 1 shows the typical cross-section of the vessels which were tested. The primary object of

the test series was to define the behavior of the end slab. The major variables were the thickness of the end slab and the magnitudes of the longitudinal and circumferential prestressing force.

Both types of structural failure of the end slabs were observed: a flexural failure and a shear failure (see Fig. 2). In the flexural failure the end slab breaks into wedge shaped segments which pivot about the outer edge. The vessel ultimately fails by fracture of the circumferential prestressing. The end slab deflection at failure is considerable. A numerical solution to the flexural failure has been obtained using the lumped-parameter model (3). The elastic-crack solution presented in Reference 3 predicts with reasonable tolerances the physical behavior of the test vessel.

In the shear failure inclined cracks develop in the end slab at about middepth of the slab. These cracks propagate toward the top and bottom of the slab. The vessel fails as a result of the failure of the concrete near the end of the inclined crack. The punching failure of the circular portion of the slab at the center was abrupt. The end slab deflection was generally less for vessels failing in shear but even in these cases was still a relatively large value.

Reinforcing the end slab can improve the flexural capacity of the vessel. However, the use of reinforcement to control shear failures has been found to be ineffective for deep slabs (4). The slab in the experimental phase of the pressure vessel study was not reinforced because the presence of

reinforcement would make the understanding of the complex concrete behavior much more difficult.

Other small-scale experimental work has been performed to study the behavior of end slabs of cylindrical pressure vessels. Campbell-Allen and Low (5) conducted a series of tests on isolated circular concrete slabs with clamped edges. They obtained shear failures. Brading and Hills (6) investigated the behavior of isolated circular end slabs and end slabs with cylindrical skirt. Flexural and shear failures were observed on the isolated slabs. The cylindrical vessels failed because of excessive elongation of vertical prestressing causing circumferential crack in the wall.

Hornby, Verdon and Wong (7) tested a 1/8th scale model of the cylindrical prestressed concrete pressure vessel used for the Oldbury nuclear power station. The ultimate structural failure could not be obtained because the vessel liner failed and the pressure could not be increased. Price and Hinley (8) studied the behavior of a cylindrical concrete pressure vessel under prestress and various conditions of internal pressure and thermal loading. A plug type failure of the unreinforced end slab was obtained.

Many other investigations have been carried out in the area of prestressed concrete nuclear pressure vessels. Tan (9) has compiled an extensive bibliography of investigations conducted through 1968 on this subject.

1.2 Object and Scope

The object of this investigation is to develop an analytical procedure that would predict the crack propagation of a shear type failure in the end slab of cylindrical prestressed concrete reactor vessel. The investigation is limited to the elastic-crack solution for static loads and isothermal conditions.

The lumped-parameter model developed at University of Illinois is used in a form extended to solve the axisymmetric solid problem of the cylindrical vessel. Some of the problems which have been studied using this model are: axisymmetric solids (3), plane problems of solid media (10), shells (11, 12, 13), plates (14) and contained plastic flow (15).

The numerical problem is formulated using the displacement method of analysis where the element stiffnesses are derived by the application of the principle of virtual displacement. Displacements, strains and stresses are computed at discrete points for various stages of loading. The maximum principle strain at each point is checked for each stage of loading to determine which points if any have attained the cracking tensile strain of the concrete. New stiffness properties of an element are derived whenever a node reaches the limiting tensile strain.

A solution to a prestressed concrete vessel is obtained and it is compared with the experimental result.

1.3 Notation

The following symbols have been used throughout the text:

$[a]$	=	transformation matrix relating strains to displacements
A_{sh}	=	area of the hoop prestressing
$A_{s\ell}$	=	area of the longitudinal prestressing
$[C]$	=	elasticity matrix in the global coordinates
$[C_p]$	=	elasticity matrix in the principal directions
D	=	out to out diameter of the vessel
E_c	=	modulus of elasticity of concrete
E_s	=	modulus of elasticity of steel
H	=	total height of the vessel
k	=	a factor which extrapolates to the internal pressure causing next cracking
$k_{e\ell}$	=	an equivalent spring stiffness in the longitudinal direction
k_{er}	=	an equivalent spring stiffness in the radial direction
$[K_m]$	=	stiffness matrix of an element
L_r	=	grid length in the r-direction
L_z	=	grid length in the z-direction
ΔP	=	change in confining pressure from the hoop prestressing

R	=	radius to the element under consideration
R_o	=	radius to the exterior face of the wall
ΔT	=	change in the hoop prestressing force
u	=	displacement in the r-direction
v	=	displacement in the z-direction
ν	=	Poisson's ratio
ε_{cr}	=	concrete cracking strain in tension
$\varepsilon_1, \varepsilon_2, \varepsilon_3$	=	principal strains at a point
$\varepsilon_r, \varepsilon_z, \varepsilon_\theta, \varepsilon_{rz}$	=	strains at a point in global coordinates
$\varepsilon_r^i, \varepsilon_z^i, \varepsilon_\theta^i, \varepsilon_{rz}^i$	=	strains at a point under an applied pressure p_i
$\varepsilon_r^{pr}, \varepsilon_z^{pr}, \varepsilon_\theta^{pr}, \varepsilon_{rz}^{pr}$	=	strains at a point from prestressing
$\varepsilon_r^t, \varepsilon_z^t, \varepsilon_\theta^t, \varepsilon_{rz}^t$	=	strains at a point from prestressing and applied internal pressure p_i
$\sigma_r, \sigma_z, \sigma_\theta, \sigma_{rz}$	=	stresses at a point in the global coordinates

2. DESCRIPTION OF THE MODEL

2.1 Governing Equations

For an axisymmetric solid of revolution loaded symmetrically the deformation of the body is symmetric with respect to the axis of revolution. Referring to Fig. 3, z denotes the axis of symmetry, r the axis perpendicular to z axis and θ the central angle from an arbitrarily selected plane containing the axis of symmetry. The components of displacement in the radial and vertical directions are denoted by u and v respectively. The notations σ_r, σ_z, σ_θ, σ_{rz}, ε_r, ε_z, ε_θ, ε_{rz} are used to denote stresses and strains in r-, z-, and θ-directions.

Because of symmetry the displacement and stress components are independent of θ. Likewise all derivatives with respect to θ vanish. The strain components for small displacement theory are related to the displacements by the following equations (16):

$$\varepsilon_r = \frac{\partial u}{\partial r}, \quad \varepsilon_z = \frac{\partial v}{\partial z}, \quad \varepsilon_\theta = \frac{u}{r},$$

$$\varepsilon_{rz} = \frac{\partial u}{\partial z} + \frac{\partial v}{\partial r}, \quad \varepsilon_{r\theta} = \varepsilon_{\theta z} = 0 \tag{2.1}$$

The differential equations of equilibrium are written as:

$$\frac{\partial \sigma_r}{\partial r} + \frac{\partial \sigma_{rz}}{\partial z} + \frac{\sigma_r - \sigma_\theta}{r} = 0 \tag{2.2}$$

for the r-direction, and

$$\frac{\partial \sigma_z}{\partial z} + \frac{\partial \sigma_{rz}}{\partial r} + \frac{\sigma_{rz}}{r} = 0 \qquad (2.3)$$

for the z-direction.

2.2 Selection of Analytical Method

The solution of the governing equations complete with satisfaction of boundary conditions is impractical for most axisymmetric solid problems. The numerical methods available for solving pressure vessel problems are the lumped-parameter (a solution procedure similar to finite difference and dynamic relaxation) and the finite element methods. The choice between these methods will depend on following factors:

a. Ability of the chosen method to predict areas of high stress concentration.

b. Ability of the method to permit simulated cracks to propagate naturally through concrete without undue influence from element geometry and arrangement selected to approximate the structure.

c. Simplicity.

The finite element method has been applied to solve problems of axisymmetric solids of revolution (17, 18, 19, 20, 21). In this method the continuous body is subdivided into triangular or quadrilateral ring elements. Then the displacements and in some cases derivatives of the displacements are defined at the nodes as shown in Fig. 4a. An equilibrium

equation (really an equation relating the internal and external work) is written for each degree of freedom yielding a set of linear algebraic equations. This procedure reduces the problem from that of solving a system of differential equations to that of solving a set of linear algebraic equations. For the displacement model, only forced (geometric) boundary conditions can be treated. Since natural (stress) boundary conditions do not enter into the formulation of the problem, the boundary conditions are simply treated by including or deleting the appropriate degrees of freedom as represented by the nodal displacements.

In using the linear displacement triangular ring element the meridian plane stresses are constant over the element. Thus stresses computed at a node point are different for all the various elements meeting at that node. One interpretation for evaluating the stresses at a node is obtained by averaging the nodal stresses. Another interpretation is to assign the computed stresses to the centroid of an element. The latter interpretation results in a certain amount of oscillations of stress values between elements and is in general a poorer approximation than the averaging of the nodal stresses. Other averaging methods have been tried. The best averaging procedure seems to be to average the stresses for two elements and prescribe that stress to a point on the line joining the centroids of the two elements (22). Due to the averaging process, there is some question regarding the accuracy of stresses and the finite

element method may not be able to find small variations in the tensile stresses in a field of high compression forces. Also there is the question of what stress or strain, centroidal or average, is to be used to establish the cracking state. Depending on the arrangement of the triangular elements, the behavior of the structure is biased in a particular direction, a factor which may affect the path of the simulated crack propagation. These comments are not so much a condemnation of the finite element method as a declaration of the sensitivity of the problem. Rashid (24) employed the linear displacement triangular ring elements to obtain a cracking solution for a pressure vessel.

Argyris et al (23) have developed various higher order displacement elements for axisymmetric problems. They have successfully applied these elements to solve elastic problems. There is no literature available to indicate that these elements have been used to solve cracking problems.

The lumped-parameter method has also been used to solve problems of axisymmetric solids of revolution (3). In this method the continuous structure is divided into a system of subregions. The behavior of the subregions is approximated by assuming that the strain quantities are constant across each subregion. Stress nodes alternate with displacement nodes in each coordinate direction in the manner indicated in Fig. 4b. Physically, the structure may be visualized as represented by a system of rigid bars interconnected by a series of deformable

nodes. In contrast to the triangular ring element of the finite element method, the lumped-parameter procedure is free of bias due to elemental arrangement. Also, there is no ambiguity in stresses because they are defined at a given node.

Based on the reasons cited above and past experience with the model, the lumped-parameter method was selected as the anayltical model to be employed for the study of elastic-crack problem in this investigation.

2.3 Details of Model

The lumped-parameter model can be described as a network of bars with stress nodes and displacement nodes alternating along grid lines in each direction (Fig. 7). The bars connecting the stress nodes are assumed rigid and all deformations are defined at the stress nodes. It is only at these nodes that the stresses and strains are considered. The horizontal, r, and vertical, z, displacements are prescribed at the displacement nodes. On the r-z plane each stress node away from the boundary is bounded by four displacement nodes and each displacement node by four stress nodes.

2.4 Strain-Displacement Relations

Employing the notations shown in Figs. 7 and 8, the strains are expressed in terms of displacements by considering all deformations between displacement points concentrated at the stress node. A uniform grid length is used in each coordinate

direction. The strains in the coordinate directions are

$$\begin{aligned} \varepsilon_r &= \frac{1}{L_r}(u_4 - u_2) \\ \varepsilon_z &= \frac{1}{L_z}(v_3 - v_1) \\ \varepsilon_\theta &= \frac{1}{2R}(u_4 + u_2) \\ \varepsilon_{rz} &= \frac{1}{L_r}(v_4 - v_2) + \frac{1}{L_z}(u_3 - u_1) \end{aligned} \tag{2.4}$$

where L_r is the distance between two adjacent stress (displacement) nodes in r-direction,

L_z is the distance between two adjacent stress (displacement) nodes in z-direction,

u_1, u_2, u_3, u_4 are the components of displacement in r-direction at displacement nodes bounding a stress node,

v_1, v_2, v_3, v_4 are the components of displacement in z-direction at displacement nodes bounding a stress-node, and

R is the radius from the axis of revolution to the stress node.

The displacement components represent the corresponding displacements at the same points in the real structure. They represent mathematically the first order central finite difference expressions for the usual strain-displacement relations for the continuum.

Equation 2.4 can be expressed in matrix form by

$$\{\varepsilon\} = [a]\{u\} \tag{2.5}$$

where

$$\{\varepsilon\} = \begin{Bmatrix} \varepsilon_r \\ \varepsilon_z \\ \varepsilon_\theta \\ \varepsilon_{rz} \end{Bmatrix},$$

$$[a] = \begin{bmatrix} 0 & 0 & -\frac{1}{L_r} & 0 & 0 & 0 & \frac{1}{L_r} & 0 \\ 0 & -\frac{1}{L_z} & 0 & 0 & 0 & \frac{1}{L_z} & 0 & 0 \\ 0 & 0 & \frac{1}{2R} & 0 & 0 & 0 & \frac{1}{2R} & 0 \\ -\frac{1}{L_z} & 0 & 0 & -\frac{1}{L_r} & \frac{1}{L_z} & 0 & 0 & \frac{1}{L_r} \end{bmatrix}, \text{ and}$$

$$\{u\} = (u_1 \quad v_1 \quad u_2 \quad v_2 \quad u_3 \quad v_3 \quad u_4 \quad v_4)^T$$

2.5 Material Properties

Two materials, concrete and steel, are the structural components of the prestressed concrete pressure vessels. In contrast to the flexural failure, the shear failure is directly related to concrete properties. Therefore, a reliable triaxial failure criterion for concrete subjected to combinations of tensile and compressive stresses becomes important.

Numerous experiments have been conducted to determine the behavior of concrete under multiaxial state of stresses (25, 26, 27, 28, 29). Most of the experimental work performed thus far have been limited to biaxial and triaxial compression tests.

Much work has been performed with the objective pointed toward the development of a failure criterion for concrete. However, no data exist relative to the stress-strain characteristics for the multiaxial case. Hannant and Frederick (30) have evaluated the results of several investigators and developed a failure criterion for concrete in biaxial and triaxial compression. The failure of concrete is described in terms of failure surfaces in three-dimensional stress space of concrete subjected to multiaxial compression. Another theory available is the Mohr's failure criterion which is applicable to concrete in biaxial and triaxial compression. But as yet, there is no general triaxial failure criterion for concrete subjected to combinations of tensile and compressive stresses.

For lack of a general triaxial failure criterion, the maximum tensile strain theory was adopted as the failure criterion for concrete in this investigation. There is a scarcity of information pertinent to the cracking strain of concrete under multiaxial states of stress. The cracking strain value of 0.0003 was adopted on the basis of the strains measured during the test of the small scale vessel.

A linear stress-strain curve is assumed for concrete although it is known that the concrete in some localized portions

of the pressure vessel will be subjected to sufficiently high stresses that some form of nonlinear behavior is possible. The assumption of a linear stress-strain relationship for the full range of stresses was made for the following reasons:

a. The portion of the cross-section subjected to stress magnitudes greater than the ultimate uniaxial compressive stress of concrete is small and localized. In addition the high compressive region is near the bottom of the slab where the multiaxial compressive stresses exist. The concrete in that region is expected therefore to remain linear beyond the attainment of maximum compressive stresses in excess of the ultimate uniaxial compressive stress (f_c').

b. The mathematical model is stable to about 70-80 % of the ultimate load. The largest compressive stress within the vessel at 80 % of ultimate load is in the neighborhood of the ultimate uniaxial compressive stress of concrete.

The stress-strain relationship for the prestressing steel is assumed linear. This assumption is justified for this study because:

a. The experiment shows that prestressing remained linear up to about 75 % of the ultimate load.

b. The mathematical model is not applicable beyond about 70-80 % of the ultimate load because at that loading the mathematical model becomes unstable.

The mathematical instability occurs when a zero term appears on the main diagonal of the structure's stiffness matrix. At that point the stiffness matrix becomes singular and no solution is possible.

2.6 General Stress-Strain Relationship

The general stress-strain relations for the axisymmetric solids of revolution may be expressed in the following matrix notations:

$$\{\sigma\} = [C]\{\varepsilon\} \tag{2.6}$$

where

$$\{\sigma\} = \begin{Bmatrix} \sigma_r \\ \sigma_z \\ \sigma_\theta \\ \sigma_{rz} \end{Bmatrix},$$

$$[C] = \begin{bmatrix} C_{11} & C_{12} & C_{13} & C_{14} \\ C_{21} & C_{22} & C_{23} & C_{24} \\ C_{31} & C_{32} & C_{33} & C_{34} \\ C_{41} & C_{42} & C_{43} & C_{44} \end{bmatrix}, \text{ and}$$

$$\{\varepsilon\} = \begin{Bmatrix} \varepsilon_r \\ \varepsilon_z \\ \varepsilon_\theta \\ \varepsilon_{rz} \end{Bmatrix}$$

2.7 Elastic Stress-Strain Relationship

The stress-strain law for the homogeneous and linearly elastic, isotropic material is given by Hooke's Law. For plane strain problems of axisymmetric solids of revolution the stress-strain relations are given in matrix form as:

$$\begin{Bmatrix} \sigma_r \\ \sigma_z \\ \sigma_\theta \\ \sigma_{rz} \end{Bmatrix} = \frac{E_c}{(1+\nu)(1-2\nu)} \begin{bmatrix} 1-\nu & \nu & \nu & 0 \\ \nu & 1-\nu & \nu & 0 \\ \nu & \nu & 1-\nu & 0 \\ 0 & 0 & 0 & \frac{1}{2}(1-2\nu) \end{bmatrix} \begin{Bmatrix} \varepsilon_r \\ \varepsilon_z \\ \varepsilon_\theta \\ \varepsilon_{rz} \end{Bmatrix}$$

or symbolically as:

$$\begin{Bmatrix} \sigma_r \\ \sigma_z \\ \sigma_\theta \\ \sigma_{rz} \end{Bmatrix} = \begin{bmatrix} B_{11} & B_{12} & B_{13} & B_{14} \\ B_{21} & B_{22} & B_{23} & B_{24} \\ B_{31} & B_{32} & B_{33} & B_{34} \\ B_{41} & B_{42} & B_{43} & B_{44} \end{bmatrix} \begin{Bmatrix} \varepsilon_r \\ \varepsilon_z \\ \varepsilon_\theta \\ \varepsilon_{rz} \end{Bmatrix} \qquad (2.7)$$

where E_c is the modulus of elasticity for concrete and ν is the Poisson's ratio.

2.8 Treatment of Concrete Cracking

In an axisymmetric solid of revolution two types of crack formation are possible:

a. A radial plane containing the longitudinal axis of the cylinder.

b. A circumferential crack symmetric about the longitudinal axis.

Figure 5 shows the radial and circumferential cracks in a differential element of the vessel.

The radial crack is formed when the circumferential strain reaches the limiting tensile strain of concrete. Because of the axial symmetry this is a principal stress direction and the evaluation of the location of the critical hoop strain is a simple matter. Similarly, the circumferential crack occurs when the maximum principal strain in the r-z plane exceeds the limiting tensile strain of concrete.

Two methods have been used by analysts in an attempt to include the effect of concrete cracking in their solution. The first of these methods involves the changing of material properties which make up the structure (3, 24). One set of material properties is assumed to exist before cracking, a second set after cracking. Prior to cracking, concrete is assumed isotropic as given in Eq. 2.7. After a node has cracked, concrete takes on orthotropic properties. The modulus in the direction normal to the crack direction is reduced to a zero value. An orthotropic material has different elastic properties in three mutually perpendicular directions as in contrast to an isotropic material whose physical properties are the same in all directions.

The alternate method is to account for cracking by changing the topology or nodal connectivity of the structure (31). This procedure is readily accomplished within the finite element

method but does restrict the cracking to following the element boundaries. When a node point cracks in the r-z plane that node splits into two nodes yielding two additional unknowns, the horizontal and the vertical displacements. Because the topology of the structure is changed whenever a node cracks the computer coding required for this method is much more complex than the material property procedure.

This alternate procedure is not possible or at least is rather ill defined within the lumped-parameter method. Since points where the deformations are defined are separated from those where the displacements are defined, the application of a stress or strain criterion to mark the separation of a displacement point into two such points is not workable.

2.9 Orthotropic Stress-Strain Relationship

When a stress node reaches the limiting tensile strain, a crack develops and the node assumes an orthotropic stress-strain relationship in the principal directions. In the direction perpendicular to the plane of the crack the stress node loses its ability to carry any force, while in the direction parallel to the plane of the crack the stress node maintains its structural capacity to resist forces. The cracking thus alters the material property matrix for the node.

The new orthotropic property matrix [C], in the r-, z- and θ-directions, can be obtained by the application of the principle of conservation of energy (24). Since energy is

independent of the coordinate system used as the reference base, the energy in the global (r,z,θ) coordinate system is equated to that of the principal directions and the following relationship is obtained:

$$\{\varepsilon\}^T \{\sigma\} = \{\varepsilon_p\}^T \{\sigma_p\} \tag{2.8}$$

where $\{\varepsilon\}$ are the strains in the global coordinate system,

$\{\sigma\}$ are the stresses in the global coordinate system,

$\{\varepsilon_p\}$ are the strains in the principal directions,

$\{\sigma_p\}$ are the stresses in the principal directions, and

$\{\varepsilon\}^T$ is the transpose of $\{\varepsilon\}$.

The stress-strain law as given by Eq. 2.6 in the global coordinate system is:

$$\{\sigma\} = [C]\{\varepsilon\} \tag{2.9}$$

Likewise, the stress-strain law written with respect to the principal directions is expressed by:

$$\begin{Bmatrix} \sigma_1 \\ \sigma_2 \\ \sigma_3 \end{Bmatrix} = \frac{E_c}{(1+\nu)(1-2\nu)} \begin{bmatrix} 1-\nu & \nu & \nu \\ \nu & 1-\nu & \nu \\ \nu & \nu & 1-\nu \end{bmatrix} \begin{Bmatrix} \varepsilon_1 \\ \varepsilon_2 \\ \varepsilon_3 \end{Bmatrix}$$

or $$\{\sigma_p\} = [C_p]\{\varepsilon_p\} \tag{2.10}$$

where σ_1 and σ_2 are the principal stresses in the r-z plane; $\sigma_3 = \sigma_\theta$, the principal stress in the hoop direction; ε_1 and ε_2

are the principal strains in the r-z plane; $\varepsilon_3 = \varepsilon_\theta$, the principal strain in the hoop direction.

The principal strains are related to strains in the global coordinates by the following well known transformation:

$$\left\{\begin{matrix}\varepsilon_1\\ \varepsilon_2\\ \varepsilon_3\end{matrix}\right\} = \begin{bmatrix}\cos^2\alpha & \sin^2\alpha & 0 & \frac{1}{2}\sin 2\alpha\\ \sin^2\alpha & \cos^2\alpha & 0 & -\frac{1}{2}\sin 2\alpha\\ 0 & 0 & 1 & 0\end{bmatrix} \left\{\begin{matrix}\varepsilon_r\\ \varepsilon_z\\ \varepsilon_\theta\\ \varepsilon_{rz}\end{matrix}\right\}$$

or $$\{\varepsilon_p\} = [T_\varepsilon]\{\varepsilon\} \qquad (2.11)$$

where T_ε is the strain transformation matrix and α is the angle between the r axis and the plane of crack (see Fig. 6). Substitution of Eqs. 2.9, 2.10 and 2.11 into Eq. 2.8 yields:

$$\{\varepsilon\}^T [C] \{\varepsilon\} = \{\varepsilon\}^T [T_\varepsilon]^T [C_p] [T_\varepsilon]\{\varepsilon\} \qquad (2.12)$$

From Eq. 2.12 the orthotropic property matrix $[C]$ in the global coordinate system is seen to be related to the matrix in the principal directions by:

$$[C] = [T_\varepsilon]^T [C_p] [T_\varepsilon] \qquad (2.13)$$

If a node cracks in the r-z plane, the first column and the first row of the matrix $[C_p]$ in Eq. 2.10 are set to zero prior to substituting into Eq. 2.13. For cracking in the radial

plane, the third column and the third row in Eq. 2.10 become zero. The orthotropic material properties for this latter case are given by:

$$[C] = \frac{E_c}{(1+\nu)(1-2\nu)} \begin{bmatrix} 1-\nu & \nu & 0 & 0 \\ \nu & 1-\nu & 0 & 0 \\ 0 & 0 & 0 & 0 \\ 0 & 0 & 0 & \frac{1}{2}(1-2\nu) \end{bmatrix} \tag{2.14}$$

When a node has cracked in the r-z and the radial planes, the only non-zero term in matrix $[C_p]$ in Eq. 2.10 is the $(1-\nu)$ term in the second row. The new orthotropic material properties are derived by substituting the revised $[C_p]$ into Eq. 2.13.

3. ELEMENT STIFFNESSES AND BOUNDARY CONDITIONS

3.1 General

The stiffness of both typical elements and those elements along the boundary are derived using the principle of virtual displacement.

Natural (stress) and geometric (forced) boundary conditions are prescribed along the edges. Actual stresses are computed along the boundary.

3.2 Stiffness Matrix of a Typical Interior Element

The principle of virtual displacement is employed in the development of an element stiffness matrix. A virtual displacement in the amount of $\{\delta u\}$ produces virtual strains of

$$\{\delta \varepsilon\} = [a] \{\delta u\} \tag{3.1}$$

Also, the external virtual work done by the loads as they experience the virtual displacement is

$$\{\delta W_e\} = \{\delta u\}^T \{P\} \tag{3.2}$$

In the same manner the internal virtual work becomes

$$\{\delta W_i\} = \int_V \{\delta \varepsilon\}^T \{\sigma\} \, dV \tag{3.3}$$

Substituting for $\{\delta\varepsilon\}$ and $\{\sigma\}$ into Eq. 3.3, following relationship is obtained:

$$\{\delta W_i\} = \int_V \{\delta u\}^T [a]^T [C] [a] \{u\} dV \qquad (3.4)$$

Equating the external virtual work to internal virtual work and cancelling $\{\delta u\}^T$ from both sides of the equation since the equality is true for arbitrary $\{\delta u\}$, an equilibrium equation for an element evolves:

$$\left(\int_V [a]^T [C] [a] dV \right) \{u\} = \{P\} \qquad (3.5)$$

Since the stresses and strains are assumed constant within a given region in the lumped-parameter model, they become independent of dV and the matrices [a] and [C] can be taken outside of the integral. Then the integration in Eq. 3.5 reduces to finding the volume integral at a given radius from the axis of revolution. The volume of the ring swept by the diamond shaped torus is easily obtained and it is equal to π R L_r L_z where R is the radius from the vertical axis of symmetry to the stress node of the element under consideration. Equation 3.5 can then be expressed in the following form:

$$\begin{bmatrix} k_{11} & k_{12} & k_{13} & \cdot & \cdot & \cdot & \cdot & k_{18} \\ k_{21} & k_{22} & k_{23} & \cdot & \cdot & \cdot & \cdot & k_{28} \\ k_{31} & k_{32} & k_{33} & \cdot & \cdot & \cdot & \cdot & k_{38} \\ \cdot & \cdot & \cdot & \cdot & \cdot & \cdot & \cdot & \cdot \\ \cdot & \cdot & \cdot & \cdot & \cdot & \cdot & \cdot & \cdot \\ \cdot & \cdot & \cdot & \cdot & \cdot & \cdot & \cdot & \cdot \\ \cdot & \cdot & \cdot & \cdot & \cdot & \cdot & \cdot & \cdot \\ k_{81} & k_{82} & k_{83} & \cdot & \cdot & \cdot & \cdot & k_{88} \end{bmatrix} \begin{Bmatrix} u_1 \\ v_1 \\ u_2 \\ v_2 \\ u_3 \\ v_3 \\ u_4 \\ v_4 \end{Bmatrix} = \begin{Bmatrix} P_{r1} \\ P_{z1} \\ P_{r2} \\ P_{z2} \\ P_{r3} \\ P_{z3} \\ P_{r4} \\ P_{z4} \end{Bmatrix}$$

or $$\left[\bar{K}_m\right] \{u\} = \{P\} \qquad (3.6)$$

See Appendix for the element stiffness of a typical interior element.

The lumped-parameter model used by Echeverria and Schnobrich (3) corresponds to the central finite difference form of the equilibrium equations. However, the model as formulated in that study requires special equations be developed to handle each different boundary condition. The stiffness method presented here does not correspond to a central finite difference equation. The reason for this deviation is because in the stiffness method the circumferential stress could not be prescribed at the centroid of the differential element. It was possible to do this in the procedure used in Reference 3. Nevertheless, the compensating advantage of the stiffness method is the ease with which the different boundary conditions can be handled.

3.3 Boundary Conditions

3.3.1 General

Those stress and displacement nodes occurring on the bounding surfaces of the vessel being analyzed require special consideration. The behavior and movement of these points are governed by the natural and geometric boundary conditions associated with corresponding surfaces of the pressure vessel. The natural boundary conditions for the axisymmetric pressure vessel problem represent conditions on the stress quantities and are treated by setting the stress normal to boundary surface equal to the applied pressure. In the pressure vessel problem the applied pressure is either the internal applied pressure or the equivalent pressure resulting from the prestressing. This in effect achieves an alteration of the stress-strain characteristics of those stress nodes which lie on the boundaries. In physical terms this represents the influence on the Poisson effect for the boundary nodes.

The geometric boundary conditions are handled by either deleting from the structure's stiffness matrix the appropriate columns and rows corresponding to zero displacements or by writing the appropriate equations expressing the interrelations of displacement components.

3.3.2 Along the Vertical Axis of Symmetry

On the vertical axis of symmetry only vertical displacements are permitted. This restriction on the displacements

means the boundary condition becomes

$$u = 0 \tag{3.7}$$

Symmetry also requires that the shear stress be equal to zero for a second, in this case natural, boundary condition:

$$\sigma_{rz} = 0 \tag{3.8}$$

Considering the boundary conditions and referring to Figs. 7 and 9, the following relations are obtained:

$$\begin{aligned} u_1 &= u_3 = 0 \\ u_2 &= -u_4 \\ v_2 &= v_4 \end{aligned} \tag{3.9}$$

Taking Eq. 3.9 into consideration, the strain-displacement relations for a stress node on the vertical axis become

$$\begin{aligned} \varepsilon_r &= \frac{2}{L_r} u_4 \\ \varepsilon_z &= \frac{1}{L_z} (v_3 - v_1) \\ \varepsilon_\theta &= \varepsilon_r \\ \varepsilon_{rz} &= 0 \end{aligned} \tag{3.10}$$

The equality of ε_θ and ε_r on the vertical axis can be shown by investigating the limit of the strain-displacement relations of small displacement theory:

$$\varepsilon_r = \frac{\partial u}{\partial r}$$

$$\varepsilon_\theta = \frac{u}{r}$$

as r goes to zero,

$$\varepsilon_\theta = \lim_{r \to 0} \left(\frac{u}{r}\right) = \lim_{r \to 0} \left(\frac{\partial u/\partial r}{\partial r/\partial r}\right)$$

$$\varepsilon_\theta = \frac{\partial u}{\partial r} = \varepsilon_r$$

The strain-displacement relationship applicable to stress nodes on the center line thus simplifies to

$$\begin{Bmatrix} \varepsilon_r \\ \varepsilon_z \\ \varepsilon_\theta \end{Bmatrix} = \begin{bmatrix} 0 & 0 & \frac{2}{L_r} \\ -\frac{1}{L_z} & \frac{1}{L_z} & 0 \\ 0 & 0 & \frac{2}{L_r} \end{bmatrix} \begin{Bmatrix} v_1 \\ v_3 \\ u_4 \end{Bmatrix} \quad \text{or } \{\varepsilon\} = [a]\ \{u\} \qquad (3.11)$$

The stress-strain relationship with the shear strain deleted reduces to

$$\begin{Bmatrix} \sigma_r \\ \sigma_z \\ \sigma_\theta \end{Bmatrix} = \begin{bmatrix} C_{11} & C_{12} & C_{13} \\ C_{21} & C_{22} & C_{23} \\ C_{31} & C_{32} & C_{33} \end{bmatrix} \begin{Bmatrix} \varepsilon_r \\ \varepsilon_z \\ \varepsilon_\theta \end{Bmatrix} \quad \text{or } \{\sigma\} = [C]\ \{\varepsilon\} \qquad (3.12)$$

Substituting [a] and [C] from the above relations into Eq. 3.5, the stiffness for an element where the stress node lies on the

vertical symmetry is obtained. The Appendix lists the terms in the stiffness matrix for this type of element.

3.3.3 Along the Top of Slab

Along the top of the slab the boundary is free of normal and shear stresses, that is

$$\sigma_z = 0 \qquad \text{and} \qquad \sigma_{rz} = 0 \tag{3.13}$$

Since σ_z is equal to zero, ε_z can be expressed in terms of ε_r and ε_θ. Then from stress-strain relations, Eq. 2.7, ε_z becomes

$$\varepsilon_z = -\frac{B_{21}}{B_{22}}\varepsilon_r - \frac{B_{23}}{B_{22}}\varepsilon_\theta \tag{3.14}$$

Substituting ε_z from Eq. 3.14 into σ_r and σ_θ of Eq. 2.7, the following stress-strain relations are obtained:

$$\begin{aligned}
\sigma_r &= \left(B_{11} - \frac{B_{12}\,B_{21}}{B_{22}}\right)\varepsilon_r + \left(B_{13} - \frac{B_{12}\,B_{23}}{B_{22}}\right)\varepsilon_\theta \\
\sigma_\theta &= \left(B_{31} - \frac{B_{32}\,B_{21}}{B_{22}}\right)\varepsilon_r + \left(B_{33} - \frac{B_{32}\,B_{23}}{B_{22}}\right)\varepsilon_\theta
\end{aligned} \tag{3.15}$$

In matrix notation the above equations are written as:

$$\begin{Bmatrix} \sigma_r \\ \sigma_\theta \end{Bmatrix} = \begin{bmatrix} C_{11} & C_{13} \\ C_{31} & C_{33} \end{bmatrix} \begin{Bmatrix} \varepsilon_r \\ \varepsilon_\theta \end{Bmatrix} \tag{3.16}$$

where $$C_{11} = B_{11} - \frac{B_{12}\,B_{21}}{B_{22}}$$

$$C_{13} = B_{13} - \frac{B_{12}\,B_{23}}{B_{22}}$$

$$C_{31} = B_{31} - \frac{B_{32}\,B_{21}}{B_{22}}$$

$$C_{33} = B_{33} - \frac{B_{32}\,B_{23}}{B_{22}}$$

Referring to Figs. 7 and 10, the following set of strain-displacement relations are obtained:

$$\begin{Bmatrix} \varepsilon_r \\ \varepsilon_\theta \end{Bmatrix} = \begin{bmatrix} -\frac{1}{L_r} & \frac{1}{L_r} \\ \frac{1}{2R} & \frac{1}{2R} \end{bmatrix} \begin{Bmatrix} u_2 \\ u_4 \end{Bmatrix} \qquad (3.17)$$

Incorporating these quantities into Eq. 3.5 and performing the integration, the stiffness matrix is obtained. This stiffness matrix is given in the Appendix.

3.3.4 Along the Bottom of Slab

The boundary conditions along the bottom of the slab involve specification of the levels of stress. These natural boundary conditions are

$$\sigma_z = P \quad \text{and} \quad \sigma_{rz} = 0 \qquad (3.18)$$

where p is the applied internal pressure per unit area. The vertical stress σ_z in Eq. 3.18 can be recast in terms of the

strains by using the symbols introduced in Eq. 2.7. This type of change of variable is in fact necessary because there are not sufficient displacement nodes to establish the strain from the displacement for the stress nodes on the boundary. The appropriate equation is

$$\sigma_z = B_{21}\,\varepsilon_r + B_{22}\,\varepsilon_z + B_{23}\,\varepsilon_\theta = p \ .$$

Solving for ε_z in the above equation, the following relationship is obtained in terms of ε_r, ε_θ and p.

$$\varepsilon_z = -\frac{B_{21}}{B_{22}}\,\varepsilon_r - \frac{B_{23}}{B_{22}}\,\varepsilon_\theta + \frac{1}{B_{22}}\,p \tag{3.19}$$

Substituting ε_z from Eq. 3.19 into σ_r and σ_θ of Eq. 2.7, the following stress-strain relations are attained.

$$\begin{aligned}
\sigma_r &= \left(B_{11} - \frac{B_{12}\,B_{21}}{B_{22}}\right)\varepsilon_r + \left(B_{13} - \frac{B_{12}\,B_{23}}{B_{22}}\right)\varepsilon_\theta + \frac{B_{12}}{B_{22}}\,p \\
\sigma_\theta &= \left(B_{31} - \frac{B_{32}\,B_{21}}{B_{22}}\right)\varepsilon_r + \left(B_{33} - \frac{B_{32}\,B_{23}}{B_{22}}\right)\varepsilon_\theta + \frac{B_{32}}{B_{22}}\,p
\end{aligned} \tag{3.20}$$

The coefficients of the strains in Eqs. 3.15 and 3.20 are identical. Therefore, Eq. 3.20 can be simply presented by employing the notations used in Eq. 3.16.

$$\begin{Bmatrix} \sigma_r \\ \sigma_\theta \end{Bmatrix} = \begin{bmatrix} C_{11} & C_{13} \\ C_{31} & C_{33} \end{bmatrix} \begin{Bmatrix} \varepsilon_r \\ \varepsilon_\theta \end{Bmatrix} + \frac{p}{B_{22}} \begin{Bmatrix} B_{12} \\ B_{32} \end{Bmatrix} \tag{3.21}$$

The strain-displacement relations are derived by considering the displacement components shown in Fig. 11.

$$\begin{Bmatrix} \varepsilon_r \\ \varepsilon_\theta \end{Bmatrix} = \begin{bmatrix} -\frac{1}{L_r} & \frac{1}{L_r} \\ \frac{1}{2R} & \frac{1}{2R} \end{bmatrix} \begin{Bmatrix} u_2 \\ u_4 \end{Bmatrix} \qquad (3.22)$$

This relations are identical to Eq. 3.17.

By applying the principle of virtual displacement the stiffness matrix for the element with a stress node on the bottom surface of the slab is derived. If the second term, i.e. that involving the pressure p in Eq. 3.21 is neglected, the stiffness matrix for the element on the bottom becomes exactly equal to that at the top of the slab. For a zero Poisson's ratio the B_{ij} values are zero so the pressure term vanishes from Eq. 3.21. For Poisson's ratios other than zero, however, there will be a slight error introduced in an equilibrium equation written parallel to the surface of the edge if the second or pressure term is neglected.

In this investigation the effect of the second term was neglected. This step was taken after a study showed that the effect of neglecting that term was small on the over-all behavior of the structure.

3.3.5 Along the Exterior of Wall

The stress nodes on the exterior face of the wall are subjected to an applied pressure due to prestressing. The natural boundary conditions along the wall are:

$$\sigma_r = p_e \quad \text{and} \quad \sigma_{rz} = 0 \tag{3.23}$$

where p_e is the equivalent applied pressure per unit area due to hoop prestressing. The radial stress σ_r in the above equation can be expanded as:

$$\sigma_r = B_{11}\,\varepsilon_r + B_{12}\,\varepsilon_z + B_{13}\,\varepsilon_\theta = p_e$$

Solving for ε_r in terms of ε_z, ε_θ and p_e, the following equation is obtained.

$$\varepsilon_r = -\frac{B_{12}}{B_{11}}\,\varepsilon_z - \frac{B_{13}}{B_{11}}\,\varepsilon_\theta + \frac{1}{B_{11}}\,p_e \tag{3.24}$$

The following stress-strain relations are obtained after substituting ε_r from Eq. 3.24 into σ_z and σ_θ in Eq. 2.7.

$$\begin{aligned}
\sigma_z &= \left(B_{22} - \frac{B_{12}\,B_{21}}{B_{11}}\right)\varepsilon_z + \left(B_{23} - \frac{B_{13}\,B_{21}}{B_{11}}\right)\varepsilon_\theta + \frac{B_{21}}{B_{11}}\,p_e \\
\sigma_\theta &= \left(B_{32} - \frac{B_{12}\,B_{31}}{B_{11}}\right)\varepsilon_z + \left(B_{33} - \frac{B_{13}\,B_{31}}{B_{11}}\right)\varepsilon_\theta + \frac{B_{31}}{B_{11}}\,p_e
\end{aligned} \tag{3.25}$$

By letting

$$C_{22} = B_{22} - \frac{B_{12}\,B_{21}}{B_{11}}, \qquad C_{23} = B_{23} - \frac{B_{13}\,B_{21}}{B_{11}},$$

$$C_{32} = B_{32} - \frac{B_{12}\,B_{31}}{B_{11}}, \qquad C_{33} = B_{33} - \frac{B_{13}\,B_{31}}{B_{11}},$$

Eq. 3.25 can be simply presented as:

$$\begin{Bmatrix} \sigma_z \\ \sigma_\theta \end{Bmatrix} = \begin{bmatrix} C_{22} & C_{23} \\ C_{32} & C_{33} \end{bmatrix} \begin{Bmatrix} \varepsilon_z \\ \varepsilon_\theta \end{Bmatrix} + \frac{p_e}{B_{11}} \begin{Bmatrix} B_{21} \\ B_{31} \end{Bmatrix} \tag{3.26}$$

From a study of Figs. 7 and 13, the strain-displacement relations can readily be recognized to be expressible as:

$$\begin{Bmatrix} \varepsilon_z \\ \varepsilon_\theta \end{Bmatrix} = \begin{bmatrix} -\frac{1}{L_z} & 0 & \frac{1}{L_z} \\ 0 & \frac{1}{R} & 0 \end{bmatrix} \begin{Bmatrix} v_1 \\ u_2 \\ v_3 \end{Bmatrix} \tag{3.27}$$

For the reasons given in the Section 3.3.4 the second term involving p_e in Eq. 3.26 is neglected in applying the principle of virtual displacement. The resulting element stiffness matrix is given in the Appendix.

3.3.6 Along the Interior Face of Wall

The boundary conditions and the element stiffness along the interior face of the wall are treated exactly like the exterior face of the wall.

3.3.7 Along the Horizontal Axis of Symmetry

On the horizontal axis of symmetry the vertical deflections are equal to zero and the geometric boundary condition becomes

$$v = 0 \tag{3.28}$$

Since the shear must vanish on a line of symmetry,

$$\sigma_{rz} = 0. \tag{3.29}$$

Taking symmetry into consideration and referring to Figs. 7 and 14,

$$v_1 = -v_3 \tag{3.30}$$

and the strain-displacement relationship takes the following form:

$$\begin{Bmatrix} \varepsilon_r \\ \varepsilon_z \\ \varepsilon_\theta \end{Bmatrix} = \begin{bmatrix} -\frac{1}{L_r} & 0 & \frac{1}{L_r} \\ 0 & \frac{2}{L_z} & 0 \\ \frac{1}{2R} & 0 & \frac{1}{2R} \end{bmatrix} \begin{Bmatrix} u_2 \\ v_3 \\ u_4 \end{Bmatrix}$$

The stress-strain relationship given in Eq. 2.6 reduces to following:

$$\begin{Bmatrix} \sigma_r \\ \sigma_z \\ \sigma_\theta \end{Bmatrix} = \begin{bmatrix} C_{11} & C_{12} & C_{13} \\ C_{21} & C_{22} & C_{23} \\ C_{31} & C_{32} & C_{33} \end{bmatrix} \begin{Bmatrix} \varepsilon_r \\ \varepsilon_z \\ \varepsilon_\theta \end{Bmatrix}$$

See Appendix for the stiffness matrix of this element.

4. METHOD OF ANALYSIS

4.1 Solution Process

In the lumped-parameter method an assemblage of elements replaces the continuous body. The equations necessary to carry out a numerical analysis of the pressure vessel problem are generated by performing a direct stiffness analysis of this element assemblage. When solving the equations, the proper boundary conditions are taken into account by the procedures outlined in Chapter 3.

The entire assembly and solution process was performed on the IBM 360/75 computer operated by the Department of Computer Science of the University of Illinois. At the outset the dimensions of the structure, the size of grids and the material properties of concrete and prestressing steel are input as data. The displacement node-stress node and the stress node-displacement node incidence tables are created. The numbering and ordering of the unknown displacements take place next. For the L-shaped cross section of the pressure vessels the ordering of the unknowns in the diagonal manner starting at the top of slab along the vertical axis of symmetry creates a tightly banded stiffness matrix as opposed to ordering horizontally or vertically.

The stiffness of the structure is generated and stored in the computer an equation at a time by moving diagonally across

the L-shaped cross section. This method of generating the coefficients of the equilibrium equations facilitates the modification of the coefficients in the post elastic range.

Initially, the structure is subjected to prestressing loads; the displacements, strains and stresses are computed and stored in the computer. Then the stiffness of the structure is regenerated to take account of the stiffening effect on the structure from the prestressing steel as the structure expands to withstand the applied internal pressure. The solution for the internal pressure loading p_o is obtained and it is superimposed upon the solution obtained from prestressing loads. This stage of loading is represented by the point (d_o, p_o) on Line 1 in Fig. 16.

The pressure p_1 at which the structure begins to crack is found by extrapolating along Line 1 from the previous pressure p_o. One or more nodes crack under this pressure. New material properties of the cracked nodes are obtained by the procedure outlined in Chapter 2. The coefficients of the equations affected by the cracked nodes are altered. With the pressure maintained at the level p_1, the modified equations are re-solved and the cracking status rechecked. This stage corresponds to the point (d_2, p_1) on Line 2 of Fig. 16. If more nodes crack, the coefficients of the affected equations are again modified and a solution is repeated for pressure p_1. This solution gives the point (d_3, p_1) on Line 3. If no additional

node cracks under pressure p_1, the next cracking pressure p_2 is extrapolated along Line 3 from pressure p_1.

The entire steps cited above are repeated until the lumped-parameter model becomes unstable or the desired load level is reached. The appearance of a zero on the main diagonal of the stiffness matrix is the cause of instability in the mathematical model. This does not necessarily mean that the structure has completely broken down. Physically, the structure may continue to resist loads beyond the point of mathematical instability if those zero values are for points no longer active in the structure. The appearance of zeros on the main diagonal occurs for equations describing the highly cracked region of the slab near the top center. Experiment has shown that the final load carrying mechanism is the inverted dome and the slab area near the top center is not structurally required in the final stages of loading.

In summary the elastic-crack solution is simulated by series of linear algebraic equations whose coefficients are modified as the mathematical model produces cracks at various stages of loading. This solution procedure is depicted pictorially in Fig. 16.

4.2 Extrapolating to Cracking Pressure

In Chapter 2 the two possible types of crack formations are described. One type of failure occurs along the radial plane and is directly related to the hoop strain ε_θ which is one

of the three principal strains. The second type of failure yields a circumferential crack and is created by the maximum principal strain in the r-z plane.

As mentioned earlier, the nodes are assumed to have cracked when the maximum principal strain reaches the assumed limiting concrete tensile strain. It would be advantageous to be able to extrapolate from one cracking pressure to the next as in contrast to increasing the internal pressure at a fixed rate. The fixed rate technique may result in excessive computing time since it would require more cycles to converge on the cracking pressure as compared to extrapolating in one step. The extrapolating method works only because linear stress-strain relations are assumed for the materials. If the stress depended upon the previous condition, the method of course would not be applicable. In the remainder of this section the formulae for the extrapolating factor are derived.

The status of strains existing in a node under an applied pressure p_i and prestressing load are given by:

$$\begin{aligned}
\varepsilon_r^t &= \varepsilon_r^{pr} + \varepsilon_r^i \\
\varepsilon_z^t &= \varepsilon_z^{pr} + \varepsilon_z^i \\
\varepsilon_\theta^t &= \varepsilon_\theta^{pr} + \varepsilon_\theta^i \\
\varepsilon_{rz}^t &= \varepsilon_{rz}^{pr} + \varepsilon_{rz}^i
\end{aligned} \tag{4.1}$$

where ε_r^t, ε_z^t, ε_θ^t and ε_{rz}^t are the strains at a node due to prestressing and applied internal pressure p_i,

ε_r^{pr}, ε_z^{pr}, ε_θ^{pr} and ε_{rz}^{pr} are the strains corresponding to prestressing, and

ε_r^i, ε_z^i, ε_θ^i and ε_{rz}^i are the strains corresponding to internal pressure.

The strains occurring at a cracking pressure p_{cr} can be expressed in terms of strains at pressure p_i as follows:

$$\begin{aligned} \varepsilon_r^T &= \varepsilon_r^{pr} + k\,\varepsilon_r^i \\ \varepsilon_z^T &= \varepsilon_z^{pr} + k\,\varepsilon_z^i \\ \varepsilon_\theta^T &= \varepsilon_\theta^{pr} + k\,\varepsilon_\theta^i \\ \varepsilon_{rz}^T &= \varepsilon_{rz}^{pr} + k\,\varepsilon_{rz}^i \end{aligned} \tag{4.2}$$

where ε_r^T, ε_z^T, ε_θ^T and ε_{rz}^T are the strains corresponding to prestressing and applied internal pressure p_{cr},

k is the extrapolating factor.

When the radial crack forms, the cracking condition is

$$\varepsilon_\theta^T = \varepsilon_{cr} \tag{4.3}$$

where ε_{cr} is the allowable concrete tensile strain. The factor k in this case takes the form:

$$k = \frac{\varepsilon_{cr} - \varepsilon_{\theta}^{pr}}{\varepsilon_{\theta}^{i}} \tag{4.4}$$

The maximum principal strain in the r-z plane determines the circumferential cracks. The factor k is derived for this case by investigating the maximum principal strain ε_1 and setting this value equal to ε_{cr}.

$$\varepsilon_{cr} = \varepsilon_1 = \frac{1}{2}(\varepsilon_r^T + \varepsilon_z^T) + \frac{1}{2}\sqrt{(\varepsilon_r^T - \varepsilon_z^T)^2 + (\varepsilon_{rz}^T)^2} \tag{4.5}$$

Substituting ε_r^T, ε_z^T and ε_{rz}^T from Eq. 4.2 into Eq. 4.5 and simplifying and rearranging, following quadratic equation in k evolves:

$$Ak^2 + Bk + C = 0 \tag{4.6}$$

where $A = \varepsilon_r^i \varepsilon_z^i - \frac{1}{4}(\varepsilon_{rz}^i)^2$,

$B = -\varepsilon_{cr}\varepsilon_r^i - \varepsilon_{cr}\varepsilon_z^i + \varepsilon_r^{pr}\varepsilon_z^i + \varepsilon_r^i\varepsilon_z^{pr} - \frac{1}{2}\varepsilon_{rz}^{pr}\varepsilon_{rz}^i$, and

$C = \varepsilon_{cr}^2 - \varepsilon_{cr}\varepsilon_r^{pr} - \varepsilon_{cr}\varepsilon_z^{pr} + \varepsilon_r^{pr}\varepsilon_z^{pr} - \frac{1}{4}(\varepsilon_{rz}^{pr})^2$

If a given node has not cracked yet, both Eqs. 4.4 and 4.6 are evaluated. Equation 4.4 is solved when a radial crack has occurred in the previous step; likewise, Eq. 4.6 is solved if

a circumferential crack occurred. No equation need be evaluated when a node has cracked in two directions.

The factor k to be used is the smallest positive value existing within the structure at a particular pressure p.

4.3 Stiffening Effect of Prestressing

The prestressing force from post-tensioning can be categorized into two types:

a. The force generated during prestressing operation and applied to the structure as loads.

b. The force generated as a consequence of internally applied pressure and treated analytically as an equivalent spring stiffness.

The derivation of the equivalent spring stiffness is presented in the following paragraphs. It is realized that this increase is a small percentage of the initial force; however, for a cracking analysis it may be significant.

The equivalent spring constant for the longitudinal prestressing steel is obtained by considering the formulation below:

$$k_{e\ell}\ v = \varepsilon_z\ E_s\ A_{s\ell} \tag{4.7}$$

where $k_{e\ell}$ is the equivalent spring stiffness,

v is one half of the total elongation of prestressing caused by applied internal pressure,

H is the total height of the vessel,

E_s is the modulus of elasticity of prestressing steel, and

$A_{s\ell}$ is the area of prestressing steel.

For post-tensioned system the strain ε_z is expressed as:

$$\varepsilon_z = \frac{v}{H/2} \tag{4.8}$$

Substituting this value into Eq. 4.7 and solving for $k_{e\ell}$, the equivalent spring constant for the longitudinal prestressing becomes

$$k_{e\ell} = \frac{A_{s\ell} E_s}{H/2} \tag{4.9}$$

This equivalent stiffness is distributed to the displacement nodes under the anchorage plate and added to the main diagonal elements corresponding to the vertical displacements.

The equivalent spring stiffness in the radial direction is found by considering the effect of hoop prestressing. Referring to Fig. 17, the formula below is obtained:

$$\Delta T = R_o \Delta p \tag{4.10}$$

where R_o is the original radius,

Δp is the change in confining pressure caused by hoop prestressing, and

ΔT is the change in hoop prestressing force.

As the radius of the vessel increases under increasing applied internal pressure, the strain in the hoop prestressing becomes

$$\varepsilon = \frac{2\pi (R_o + u) - 2\pi R_o}{2\pi R_o} = \frac{u}{R_o} \qquad (4.11)$$

ΔT can also be presented in terms of u as :

$$\Delta T = \frac{A_{sh} f_s}{S}$$

$$= \frac{\varepsilon E_s A_{sh}}{S}$$

$$= \frac{u E_s A_{sh}}{R_o S} \qquad (4.12)$$

In the above formulations u, S and A_{sh} are defined as:

u = the increase in radius as a result of the increase in applied pressure

S = the spacing of hoop prestressing

A_{sh} = area of hoop prestressing

Equating Eq. 4.10 to 4.12 and solving for p, a relation in terms of other variables is derived.

$$\Delta p = \frac{u E_s A_{sh}}{R_o^2 S} \qquad (4.13)$$

The equivalent stiffness in the radial direction is given by:

$$k_{er}\, u = \frac{1}{2}\,\Delta p\, R_o\, L_z$$

$$= \frac{1}{2}\,\frac{u}{R_o}\,\frac{E_s\, A_{sh}}{S}\, L_z\, R_o$$

or

$$k_{er} = \frac{E_s\, A_{sh}\, L_z}{2\, R_o\, S} \qquad (4.14)$$

5. NUMERICAL RESULTS

5.1 General

To demonstrate the applicability and adequacy of the lumped-parameter model presented in the previous chapters test specimen PV16, one of the small-scale vessels tested at the University of Illinois, is analyzed. The vessel had an outer diameter D of 3 ft. 4 in., a total height H of 6 ft. 8 in., an end slab thickness t_s of 10 in., and a wall thickness t_w of 7.5 in.

The vessel was longitudinally post-tensioned with 60 - 3/4 inch diameter Stressteel rods placed in two rows of 30 rods each. The diameters of the rows were 29 inches and 34 inches, respectively. A 1/4 inch diameter prestressing wire, wrapped around the vessel, provided the circumferential prestressing. A 1-1/4 inch thick plate at the top of the slab provided the anchorage for the longitudinal prestressing. This plate also provided additional constraint in the hoop direction as the structure expanded to resist the applied internal pressure. The modulus of elasticity of prestressing steel was taken to be 28×10^6 psi.

The concrete had an ultimate uniaxial compressive strength of 7450 psi and a modulus of elasticity of 4×10^6 psi. A tensile cracking strain of 0.0003 was adopted as the limiting value.

The magnitudes of stresses and strains are affected by the Poisson's ratio. Since concrete is assumed to have cracked when the limiting tensile strain has been reached, the analysis says the structure cracks at different levels of loading and attains different maximum loads depending on the values of Poisson's ratio. The values of 0, 0.075 and 0.15 were selected as representing a reasonable range for Poisson's ratios in concrete.

The amount of hoop constraint available influences the propagation of cracks through the structure. To study the effect of hoop constraint resulting from the anchorage plate placed at the top corner of the slab, three types or degrees of hoop constraint were investigated: Type A having a zero spring constant, Type B with a finite spring constant approximating the anchorage plate resistance, and Type C with an infinitely stiff spring which prevents the radial movement of the top, outer corner of the vessel (see Fig. 18). The vessel with Type A constraint was subdivided into 1.15 in. x 1.82 in. grids yielding 643 unknowns. The grid sizes of 2.15 in. x 2.22 in. for Types B and C constraint gave 399 unknowns.

5.2 Discussion of Results

In Figs. 19, 20 and 21 the load-deformation curves are shown for three Poisson's ratios of 0, 0.075, and 0.15, respectively. In each figure the influence of the different hoop constraints at the top, outer corner of the slab is shown. The

curves are in terms of internal pressure versus the vertical displacement of the top center of slab. The origin for the displacement corresponds to a vessel under prestressing with zero internal pressure. This datum was selected so as to have the same datum used in the experiment. The maximum load attained analytically is the internal pressure at which the mathematical model becomes unstable. A study of load-deformation curves indicates that for a given Poisson's ratio Type C always became unstable at the highest internal pressure, Type B at an intermediate pressure and Type A at the lowest pressure. For a given hoop constraint the largest pressure at the onset of instability was obtained for zero Poisson's ratio, an intermediate value for 0.075 and the smallest for 0.15.

For Type A constraint the structure remained linear up to approximately 1200 psi internal pressure. At this pressure a circumferential crack appeared at the reentrant corner and a combination of circumferential and radial cracks developed at the top center of the slab. While still at the initial cracking pressure, additional radial cracks appeared. This loading-cracking procedure was repeated as many times as necessary to obtain the maximum pressure at the onset of mathematical instability. From the load-deformation curves the maximum internal pressures are given as 1600 psi for a Poisson's ratio of 0.15 and 1840 psi for 0.075. For a Poisson's ratio of 0.0 the computation was terminated at 1650 psi because the results obtained for Poisson's ratios of 0.075 and 0.15 gave sufficient information

to evaluate the effect of Poisson's ratio on the vessel behavior. Another reason for terminating at 1650 psi was that about 10 additional minutes of expensive computer time would have been required to attain the maximum load of about 1900 to 2000 psi.

Type B constraint gave similar load-deformation curves as Type A. The structural response remained linear up to about 1300 psi internal pressure when similar cracks as in Type A constraint formed at the reentrant corner and the top center of the slab. The nonlinear portion of the load-deformation curves followed the Type A curves and reached the maximum internal pressures of 2070 psi for a Poisson's ratio of 0.0, 1970 psi for 0.075 and 1740 psi for 0.15. These pressures were approximately 125 to 200 psi higher than the maximum pressures attained for Type A constraint.

Since Type C constraint prevents the radial movement of the top, outer corner of the vessel, the behavior of the vessel is different from Types A and B. The load-deformation curves for Type C were stiffer and remained linear to internal pressures of 1800 psi for a Poisson's ratio of 0.15, 1900 psi for 0.075 and 2030 psi for 0.0. Again, the initial cracks appeared simultaneously at the reentrant corner and the top center of the slab. At the initial cracking pressure circumferential cracks propagated extensively into the area of the slab above the reentrant corner. This area is bounded by three lines: a 45° line originating at the inside edge of the anchorage plate and slanting downward toward the center of the slab; the bottom of

the slab; and an imaginary line corresponding to the extension of the inside wall line into the slab. Because many nodes cracked at the initial cracking pressure the change from a linear to a nonlinear behavior was rapid as indicated by the load-deformation curves. The maximum pressures of 2320 psi for a Poisson's ratio of 0.15, 2470 psi for 0.075 and 2570 psi for 0.0 were reached. These pressures correspond to about 80% of the ultimate pressure obtained in the experiment.

In Figs. 22, 23, 24 and 25 the stress distribution through the depth of the slab is shown for Type B constraint and a Poisson's ratio of zero. The distribution is given at following points along the slab: the vertical axis of symmetry, a radius of 8.6 inches from the center, a radius of 12.5 inches (corresponds to inner face of the wall), and the outer face of the wall. The general shape of the distribution for each kind of stress was similar for Types A and B. The Poisson's ratio did not alter the shape of the stress distribution. The status of stress is given for the initial cracking pressure of 1330 psi and the maximum pressure of 2070 psi. A close look at the radial stresses at the initial cracking pressure shows that the slab acts as a partially clamped plate with tensile stresses at the top center of the slab and at the bottom of the slab adjacent to the reentrant corner. The compressive stress fields are present at the bottom center of the slab and along the top of the slab above the reentrant corner. A comparison of stress distributions for circumferential stress at the initial cracking pressure and

the maximum pressure shows the extent of radial cracks which propagated from the top center of the slab down into the slab. The zero stresses in the slab mean that the circumferential stiffness has become zero due to cracking of the concrete. The shear stress distribution is almost parabolic for the portion of the slab between the center of the slab and inner face of the wall. In a section above the inner face of the wall the shear stress distribution is practically uniform indicating that a block shear approximation may be used to estimate the magnitude of this shear stress.

Stress distributions for Type C constraint with a Poisson's ratio of zero are presented in Figs. 26, 27, 28 and 29. Although the magnitudes of stresses differ the shapes of stress distribution at the initial cracking pressure are similar for Types A, B and C. On the other hand, the shape of stress distributions at the maximum calculated pressure for Type C differs significantly with those of Types A and B. The reason for this difference is due to the higher load levels reached in the vessel with Type C constraint. At an internal pressure greater than 70% of the ultimate load, the magnitudes of stresses and strains are high and the circumferential cracking becomes extensive.

In Figs. 30, 31, 32 and 33 the calculated strains for the Type B constraint with a Poisson's ratio of zero are compared with the measured strains. The measured and the calculated

strain values are in good agreement with each other within the range of applicability of the mathematical model.

As mentioned in Chapter 1, the two failure modes are the flexural and the shear types. For both types of failure the initial cracks are similar: the circumferential crack at the reentrant corner and the radial cracks at the top center of the slab. As the internal pressure is increased beyond the initial cracking pressure, additional circumferential and radial cracks appear. A certain combination of these cracks leads to either a flexural failure or a shear failure. Following paragraphs discuss the cracking pattern associated with each type of failure.

References 1, 2 and 3 have discussed the nature of flexural failure. The first crack to form is the circumferential crack at the reentrant corner. Then, radial cracks appear at the top central region of the slab. As the load increases, the radial cracks extend slowly downward and rapidly sideward to the outside of the cylinder. When the radial cracks have become extensive and the slab is cut into pie-shaped pieces, the crack at the reentrant corner propagates toward the outside wall, initially at about 45° from the horizontal and flattening out and turning down beyond the middle of the wall. The failure is characterized by a large upward displacement of the slab turning about the outer portion of the wall. In the experiment this prying action forced the hoop prestressing at the top of the vessel to rupture culminating in a collapse of the structure.

The crack propagation for shear type failure is investigated in this study. Figure 34 shows the cracked pattern of the vessel as computed from the mathematical model. As mentioned previously, the first cracks appeared at the reentrant corner and the top center of the slab. The cracks that formed next were the radial cracks which propagated from the center outward toward the edge and from the top downward into the central region of the slab. A further increase in internal pressure brought about the formation of circumferential cracks in the part of the slab above the reentrant corner toward the center of the slab. These cracks are principally in the 45° direction and are accompanied by radial cracks at the top. Each pressure increase causes additional circumferential and radial cracks. When the mathematical model finally fails, a series of 45° cracks has propagated through the slab. The final failure mode could not be predicted by the mathematical analysis because at a pressure of 70-80% of the ultimate load the mathematical model became unstable due to the appearance of zeros on the main diagonal, as explained in Chapter 4. The crack patterns obtained analytically, however, did confirm the occurrence of inclined cracks at about 45° from the end of the anchorage plate toward the center of the slab as reported in Reference 2.

The ultimate capacity of the vessel failing in shear is related to the strengths of the circumferential prestressing and the inverted dome carved out of the end slab. The experimental results in Reference 2 indicate that the 45° inclined cracks in

the end slab led to a formation of an inverted dome (see Fig. 35a). This inverted dome is supported by a prestressed ring beam made up of the portion of the sidewall above the horizontal cracking from the reentrant corner. Finally, the concrete failed in the dome by punching through a circular portion. Sozen, Schnobrich and Paul (32) have presented a method of calculating the ultimate load of the vessel failing in shear. The method is applicable if the shape of the dome is known or the correct shape can be assumed in advance.

As long as the prestressing remains structurally sound, the vessel will probably fail in shear after the formation of a dome in the end slab. This type of failure is likely to occur even if the radial cracks penetrated to the outside wall to form a series of three-hinged arches.

Figure 35a shows the cross section of the vessel after an idealized inclined crack has carved out an inverted dome. Points A, B and C are the assumed hinge points for the three-hinged arch illustrated in Fig. 35b. The loading on the arch comes from the sectorial area with an included angle of 12°. This angle was obtained by dividing 360° by 30, the number of rods in each row of longitudinal prestressing. Points A and B are assumed to be located 4.25 inches from the exterior face of the wall and 4 inches from the top. The horizontal dimension of 4.25 inches corresponds to the location of the resultant of the longitudinal prestressing force. The hoop prestressing in the upper 10 inches of the wall is assumed to resist the horizontal reaction from the arch.

The ultimate pressure reached in the experiment was 3200 psi. Based on this loading, the loading q on the arch becomes 21 kips/in. The horizontal reaction R_h and the vertical reaction R_v become 193 kips and 131 kips, respectively. From the assumption that the hoop prestressing in the upper 10 inches of the wall resists the horizontal reaction, the stress in 1/4 inch diameter prestressing wire becomes 180 ksi. This value is less than the ultimate stress of 230 ksi for the wire whose stress-strain curve is almost elasto-plastic. The stress in the longitudinal prestressing rod is 138 ksi based on the actual rod area of 0.475 sq. in. This value is slightly less than the yield strength of 143 ksi for Stressteel rods. The tensile strength of this rod was 165 ksi. There is therefore adequate horizontal and vertical support for the arch.

6. CONCLUSION

The development of a shear failure in the end slab of the cylindrical concrete pressure vessels can be described in terms of two stages. In the initial stage a series of 45° cracks are formed. These cracks lead to a formation of an inverted dome. The second stage is characterized by the ultimate failure of the dome that was created in the previous stage.

The objective of this investigation has been the development of an analytical method which would predict cracks similar to those associated with the formation of the inverted dome. To attain this objective a lumped-parameter method of analysis has been used.

A computer program has been developed to permit a high speed processing of the resulting equations. One of the small-scale cylindrical vessels tested at University of Illinois has been analyzed. The mathematical procedure as formulated in this study is applicable up to about 70-80% of the ultimate load obtained in the experiment. The analytical model predicts the crack patterns leading to an inverted dome, although the complete shape of the dome was not defined. The over-all structural behavior as predicted by the model, within the range of its applicability, agrees favorably with the experimental result.

The absence of information on a general failure criterion for concrete presented a problem in trying to define a failure

criterion to be used in the analytical method. For lack of anything better the maximum strain theory has been used as a failure criterion in this study. Many investigators have pointed out an urgent need for a general failure criterion in the multiaxial state of stress. In order to further refine the lumped-parameter analysis to predict the behavior of the vessel in the later stages of its failure sequence the stress-strain relations for the multiaxial case must also be established. As this information becomes available, it can be incorporated into the analysis of PCRV's.

LIST OF REFERENCES

1. Sozen, M. A., and Paul, S. L., "Structural Behavior of a Small-Scale Prestressed Concrete Reactor Vessel," Nuclear Engineering and Design, Vol. 8, 1968, pp. 403-414.

2. Paul, S. L., et al, "Strength and Behavior of Prestressed Concrete Vessels for Nuclear Reactors," Civil Engineering Studies, Structural Research Series No. 346, University of Illinois, Urbana, Illinois, July 1969.

3. Echeverria, G. A., and Schnobrich, W. C., "Lumped-Parameter Analysis of Cylindrical Prestressed Concrete Reactor Vessels," Civil Engineering Studies, Structural Research Series No. 340, University of Illinois, Urbana, Illinois, December 1968.

4. Gamble, W. L., et al, "A Study of Launch Facility Closures," A report submitted to Space and Missile Systems Organization, Air Force Systems Command, the United States Air Force, Contract No. AF04(694) - 796, University of Illinois, November 1967.

5. Campbell-Allen, D., and Low, E. W., "Pressure Tests on End Slabs for Prestressed Concrete Pressure Vessels," Nuclear Engineering and Design, Vol. 6, 1967, pp. 315-359.

6. Brading, K. F., and Hills, G., "Use of Structural Models in Developing Pressure Vessel Design," Conference on Prestressed Concrete Pressure Vessels, The Institution of Civil Engineers, London, 1968.

7. Hornby, I. W., Verdon, G. F., and Wong, Y. C., "Testing the Oldbury Vessel Model," Conference on Prestressed Concrete Pressure Vessels, The Institution of Civil Engineers, London, 1968.

8. Price, D. C., and Hinley, M. S., "Testing a 1/8th Scale Cylindrical Vessel," Conference on Prestressed Concrete Pressure Vessels, The Institution of Civil Engineers, London, 1968.

9. Tan, C. P., "Prestressed Concrete in Nuclear Pressure Vessels - A Bibliography of Current Literature," USAE Report ORNL-TM-1675, Oak Ridge National Laboratory, February 1969.

10. Galloway, J. C., and Ang, A. H., "A Generalized Lumped-Parameter Model for Plane Problems of Solid Media," Civil Engineering Studies, Structural Research Series No. 341, University of Illinois, Urbana, Illinois, November 1968.

11. Schnobrich, W. C., "A Physical Analogue for the Analysis of Cylindrical Shells," Ph.D. Thesis, University of Illinois, 1962.

12. Mohraz, B., and Schnobrich, W. C., "The Analysis of Shallow Shells by a Discrete Element System," Civil Engineering Studies, Structural Research Series No. 304, University of Illinois, Urbana, Illinois, March 1966.

13. Shoeb, N. A., and Schnobrich, W. C., "The Analysis of Elasto-Plastic Shell Structures," Civil Engineering Studies, Structural Research Series No. 324, University of Illinois, Urbana, Illinois, August 1967.

14. Lopez, L. A., "A Flexural Analysis of Elastic-Plastic Rectangular Plates," Ph.D. Thesis, University of Illinois, 1966.

15. Harper, G. N., and Ang, A. H., "A Numerical Procedure for the Analysis of Contained Flow Problems," Civil Engineering Studies, Structural Research Series No. 266, University of Illinois, Urbana, Illinois, June 1963.

16. Timoshenko, S., and Goodier, J. N., Theory of Elasticity, 2nd Ed., McGraw-Hill, New York, 1951.

17. Clough, R. W., and Rashid, Y., "Finite Element Analysis of Axisymmetric Solids," Proc. ASCE, 91, EM.1, 1965, p. 71.

18. Wilson, E. L., "Structural Analysis of Axisymmetric Solids," AIAA Journal, Vol. 3, December 1965, pp. 2269-2274.

19. Rashid, Y. R., "Analysis of Axisymmetric Composite Structures by the Finite Element Method," Nuclear Engineering and Design, Vol. 3, 1966, pp. 163-182.

20. Mohraz, B., Schnobrich, W. C., and Gupta, A. K., "A Finite Element Method for the Analysis of Nozzle Openings in Shells of Revolution," Civil Engineering Studies, Structural Research Series No. 355, University of Illinois, Urbana, Illinois, December 1969.

21. Jones, R. M., and Crose, J. G., "SAAS II - Finite Element Stress Analysis of Axisymmetric Solids with Orthotropic, Temperature-Dependent Material Properties," Aerospace Corporation, September 1968.

22. Zienkiewicz, O. C., and Cheung, Y. K., The Finite Element Method in Structural and Continuum Mechanics, McGraw-Hill, 1967.

23. Argyris, J. H., et al, "Application of the Matrix Displacement Method to the Analysis of Pressure Vessels," Journal of Engineering for Industry, Transactions of the ASME, May 1970, pp. 317-329.

24. Rashid, Y. R., "Ultimate Strength Analysis of Prestressed Concrete Reactor Vessels," Nuclear Engineering and Design, Vol. 17, No. 4, April 1968.

25. Bellamy, C. J., "Strength of Concrete Under Combined Stresses," ACI Journal, Proceedings, Vol. 58, No. 4, October 1961.

26. Bresler, B., and Pister, K. S., "Strength of Concrete Under Combined Stresses," ACI Journal, Proceedings, Vol. 55, No. 3, September 1958.

27. McHenry, D., and Karni, J., "Strength of Concrete Under Combined Tensile and Compressive Stress," ACI Journal, Proceedings, Vol. 54, No. 10, September 1958.

28. Richart, F. E., Brandtzaeg, A., and Brown, R. L., "A Study of the Failure Mechanism of Concrete Under Combined Stresses," Bulletin 185, Engineering Experiment Station, University of Illinois, 1928.

29. Kupfer, H., Hilsdorf, H. K., and Rusch, H., "Behavior of Concrete Under Biaxial Stresses," ACI Journal, Proceedings, Vol. 66, No. 8, August 1969.

30. Hannant, D. J., and Frederick, C. O., "Failure Criteria for Concrete in Compression," Magazine of Concrete Research (London), Vol. 20, No. 64, September 1968.

31. Ngo, D., and Scordelis, A. C., "Finite Element Analysis of Reinforced Concrete Beams," ACI Journal, Proceedings, Vol. 64, No. 3, March 1967.

32. Sozen, M. A., Schnobrich, W. C., and Paul, S. L., "Shear Failures in the End Slabs of Prestressed Concrete Pressure Vessels," An Interim Report to AEC, University of Illinois, April 1970.

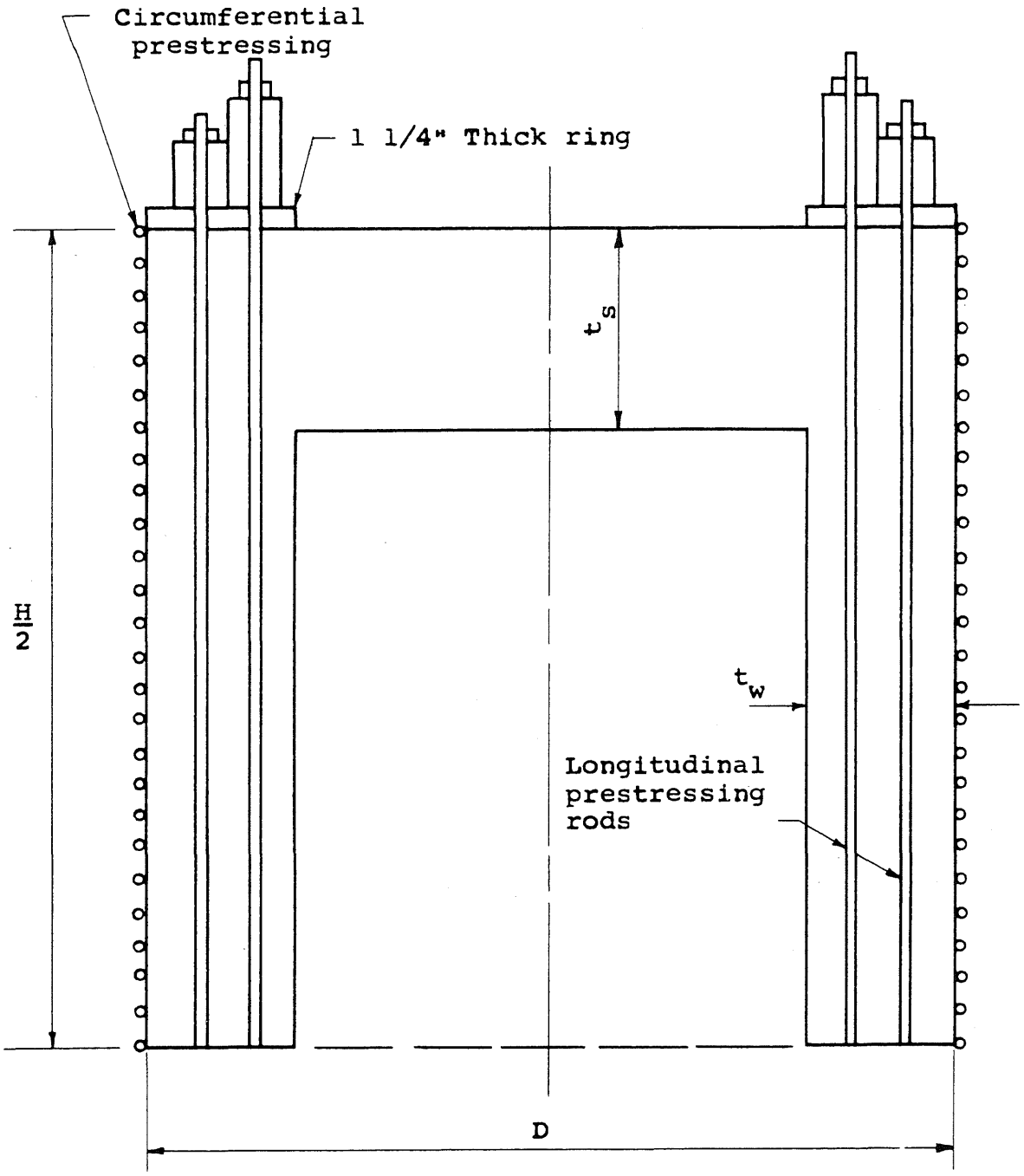

FIGURE 1. LONGITUDINAL SECTION OF THE VESSEL

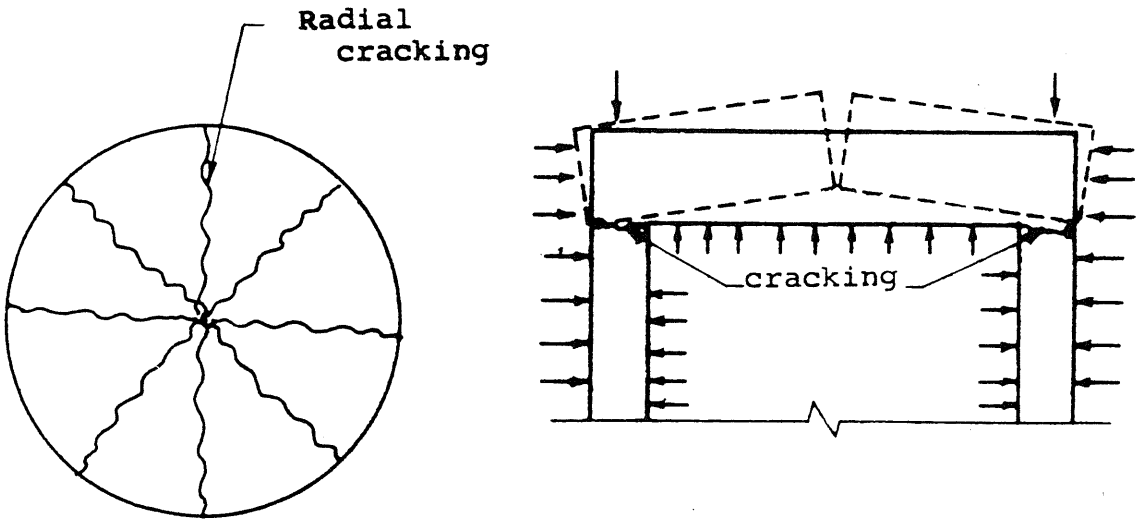

CRACKS FOR FLEXURAL FAILURE

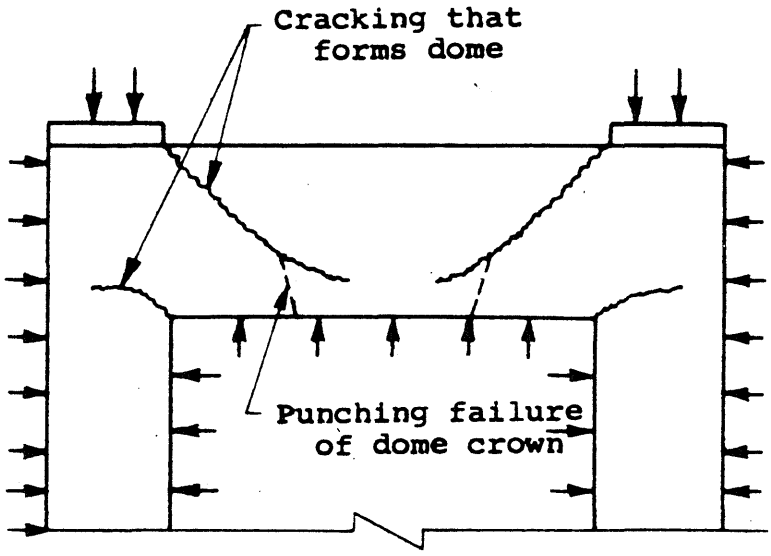

CRACKS FOR SHEAR FAILURE

FIGURE 2. IDEALIZED DEFORMATION OF VESSEL

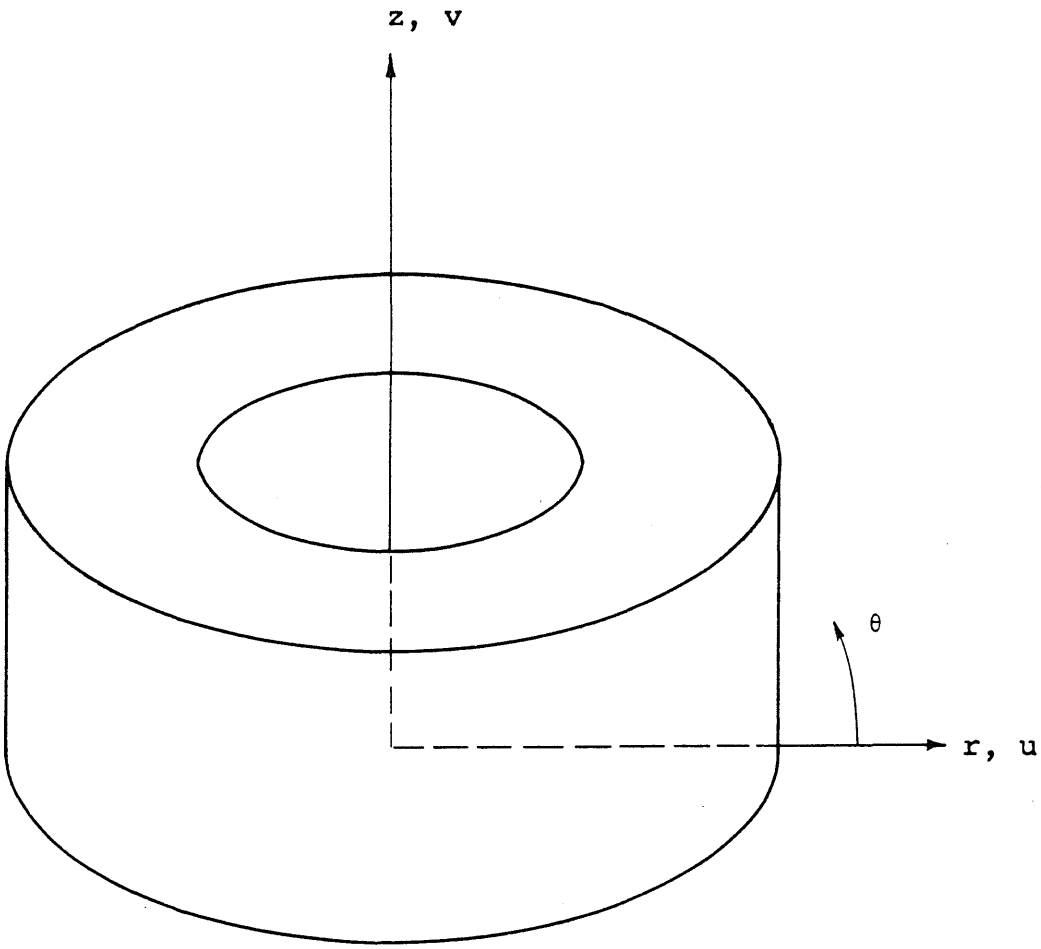

FIGURE 3. AXISYMMETRIC BODY

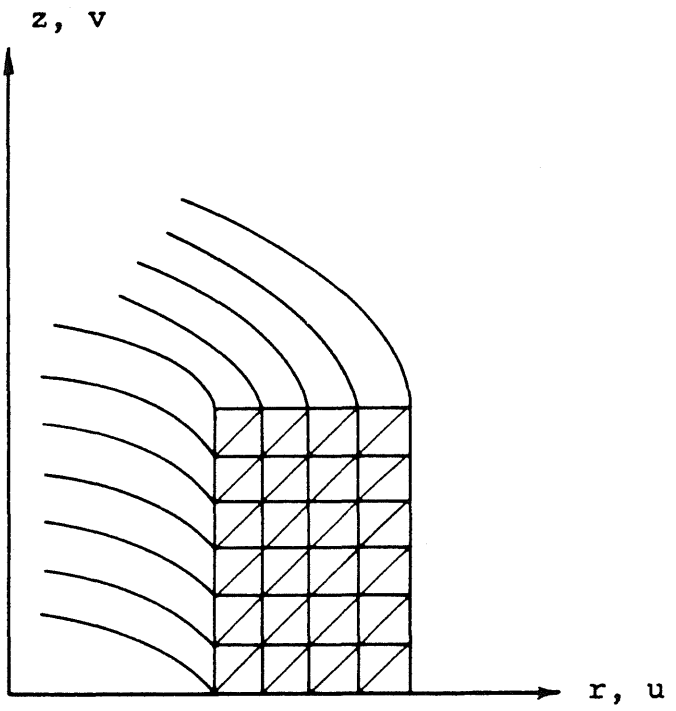

FIGURE 4a. FINITE ELEMENT IDEALIZATION

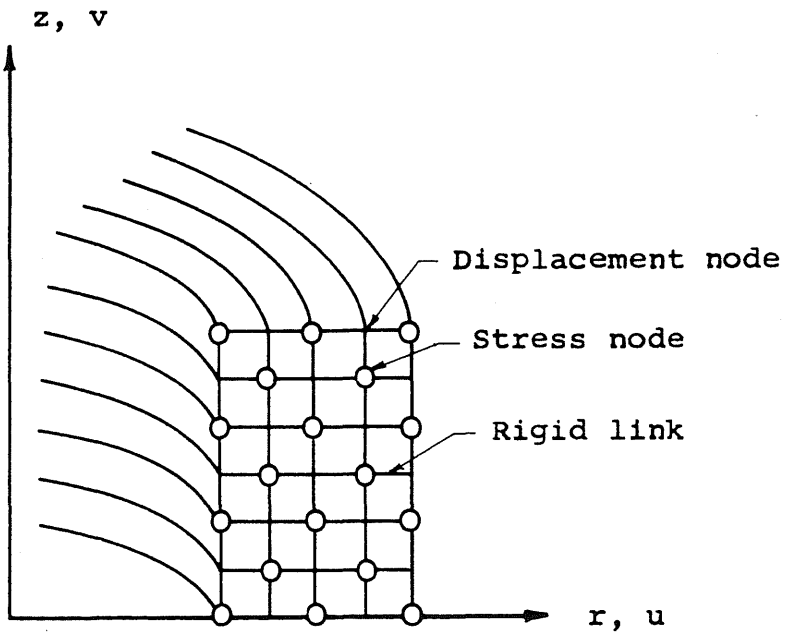

FIGURE 4b. LUMPED-PARAMETER IDEALIZATION

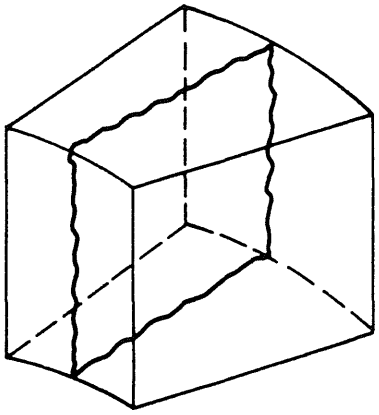

RADIAL CRACK

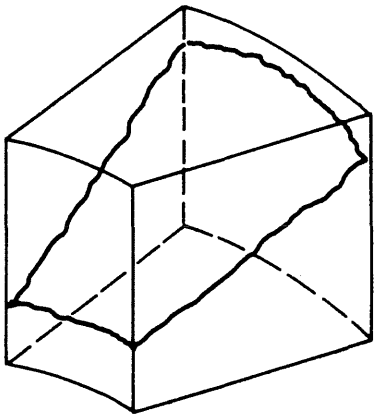

CIRCUMFERENTIAL CRACK

FIGURE 5. TYPES OF CRACK FORMATION

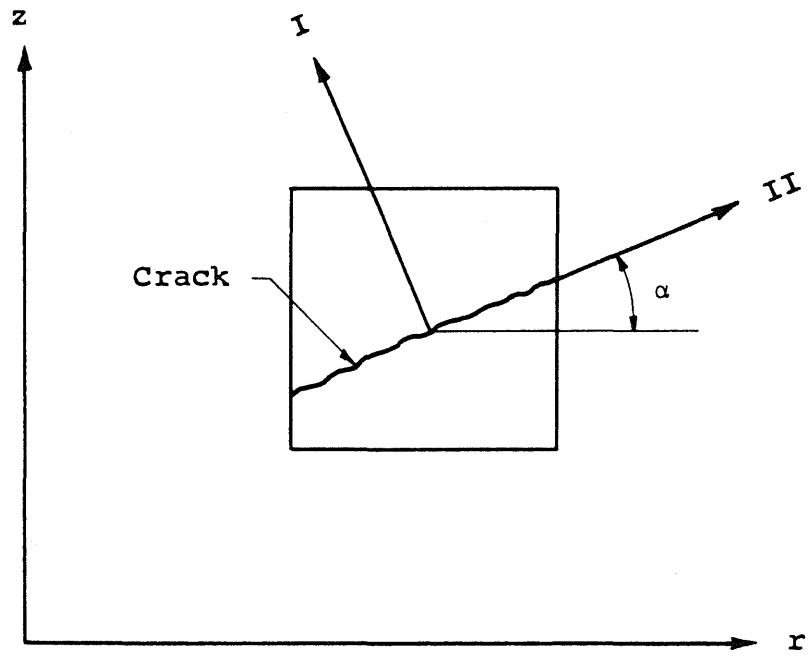

FIGURE 6. DIRECTION OF CIRCUMFERENTIAL CRACK

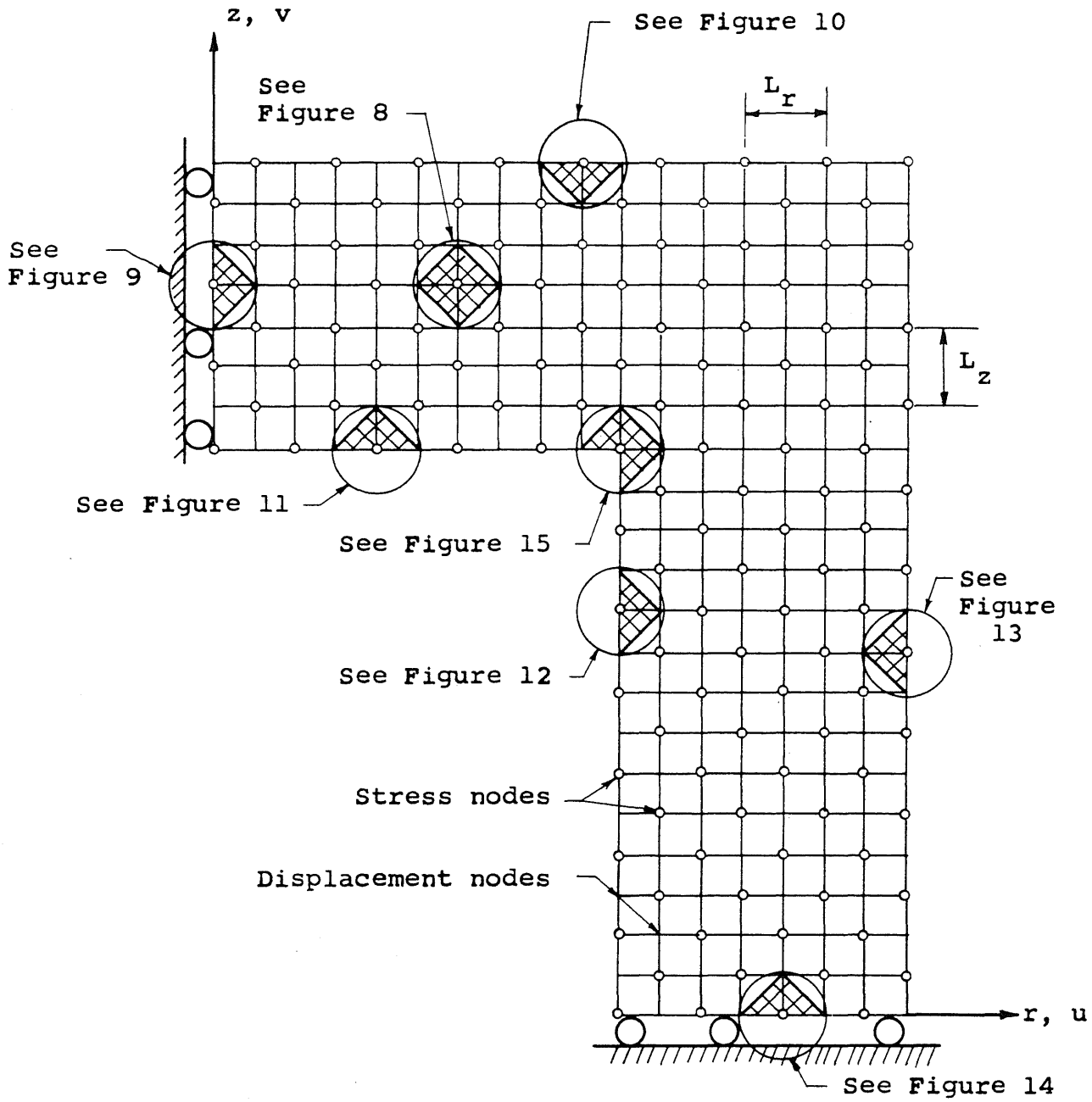

FIGURE 7. LUMPED-PARAMETER REPRESENTATION OF THE PRESSURE VESSEL

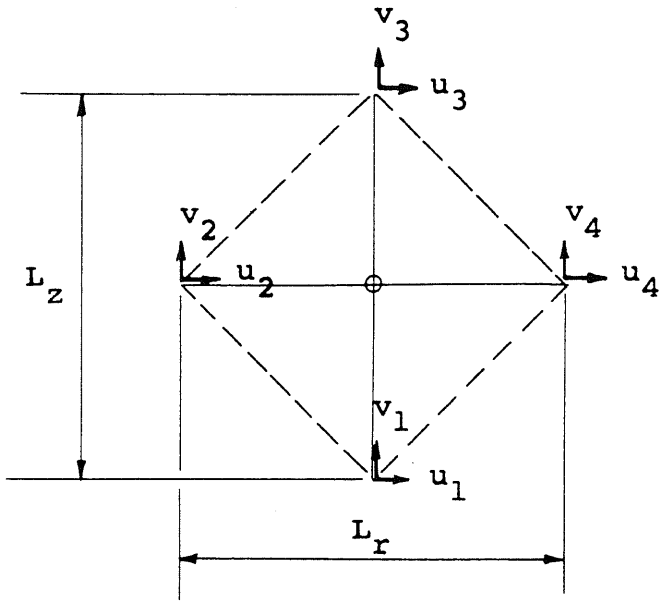

FIGURE 8. TYPICAL ELEMENT

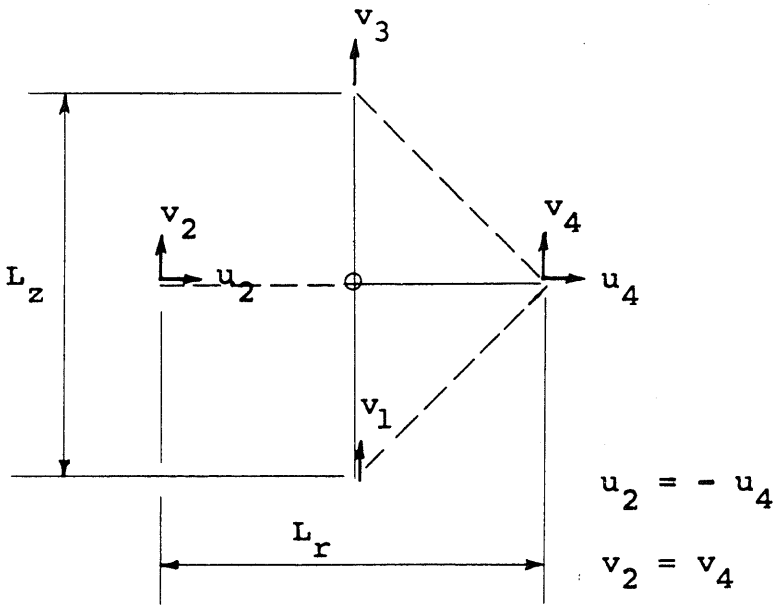

FIGURE 9. ELEMENT AT VERTICAL AXIS OF SYMMETRY

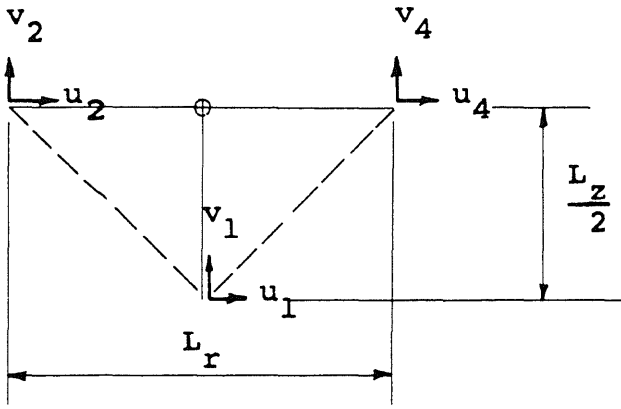

FIGURE 10. ELEMENT AT TOP OF SLAB

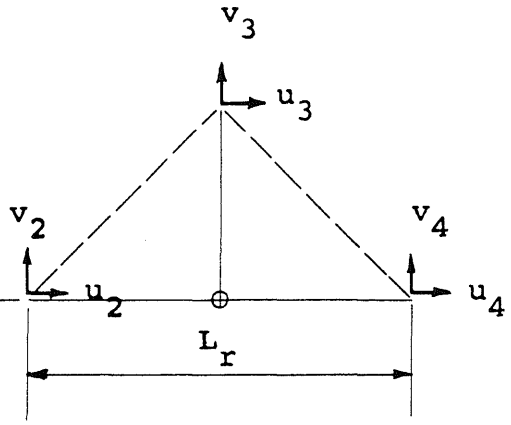

FIGURE 11. ELEMENT AT BOTTOM OF SLAB

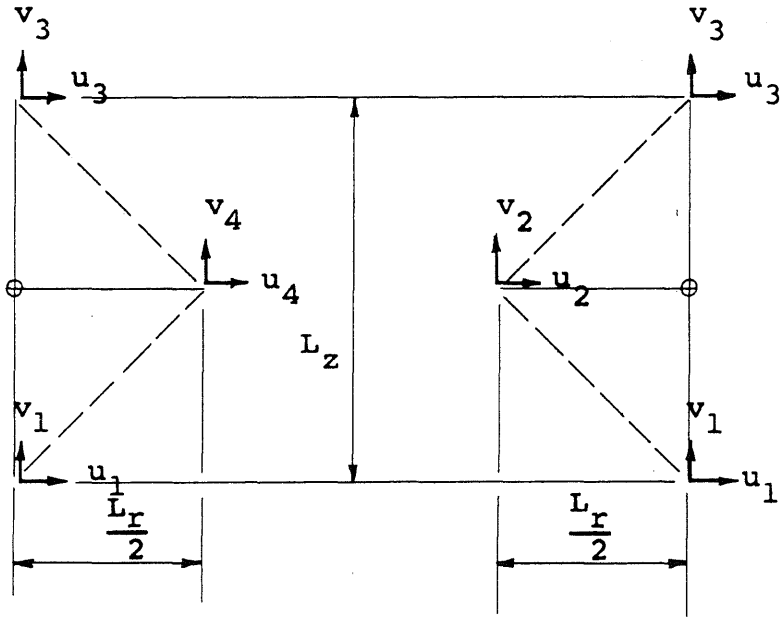

FIGURE 12. ELEMENT AT INTERIOR OF WALL

FIGURE 13. ELEMENT AT EXTERIOR OF WALL

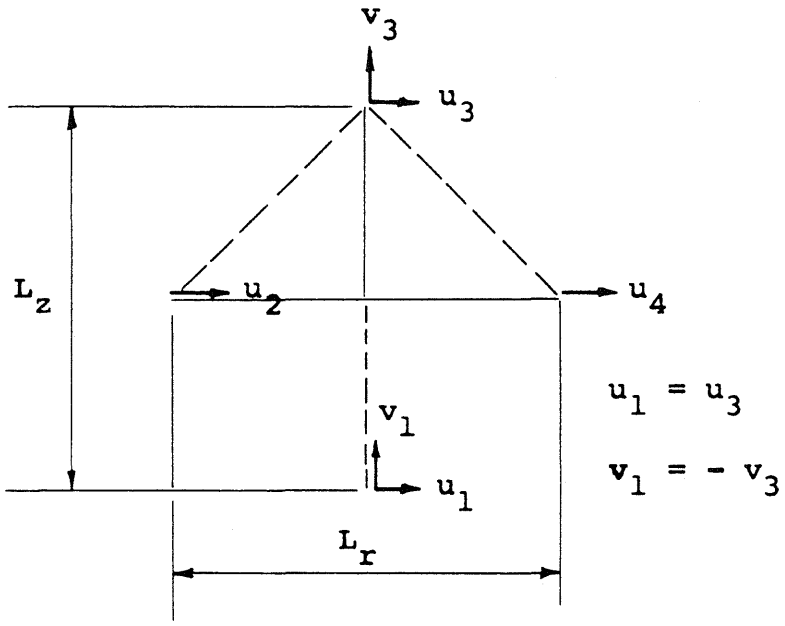

FIGURE 14. ELEMENT AT HORIZONTAL AXIS OF SYMMETRY

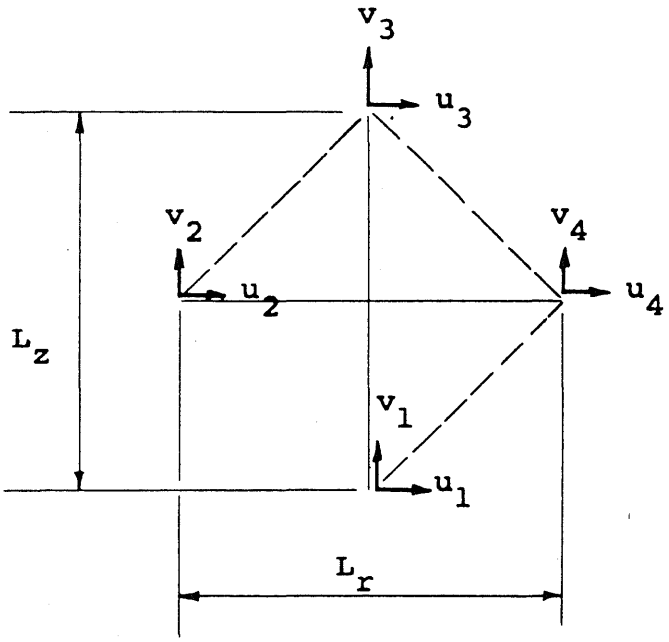

FIGURE 15. ELEMENT AT REENTRANT CORNER

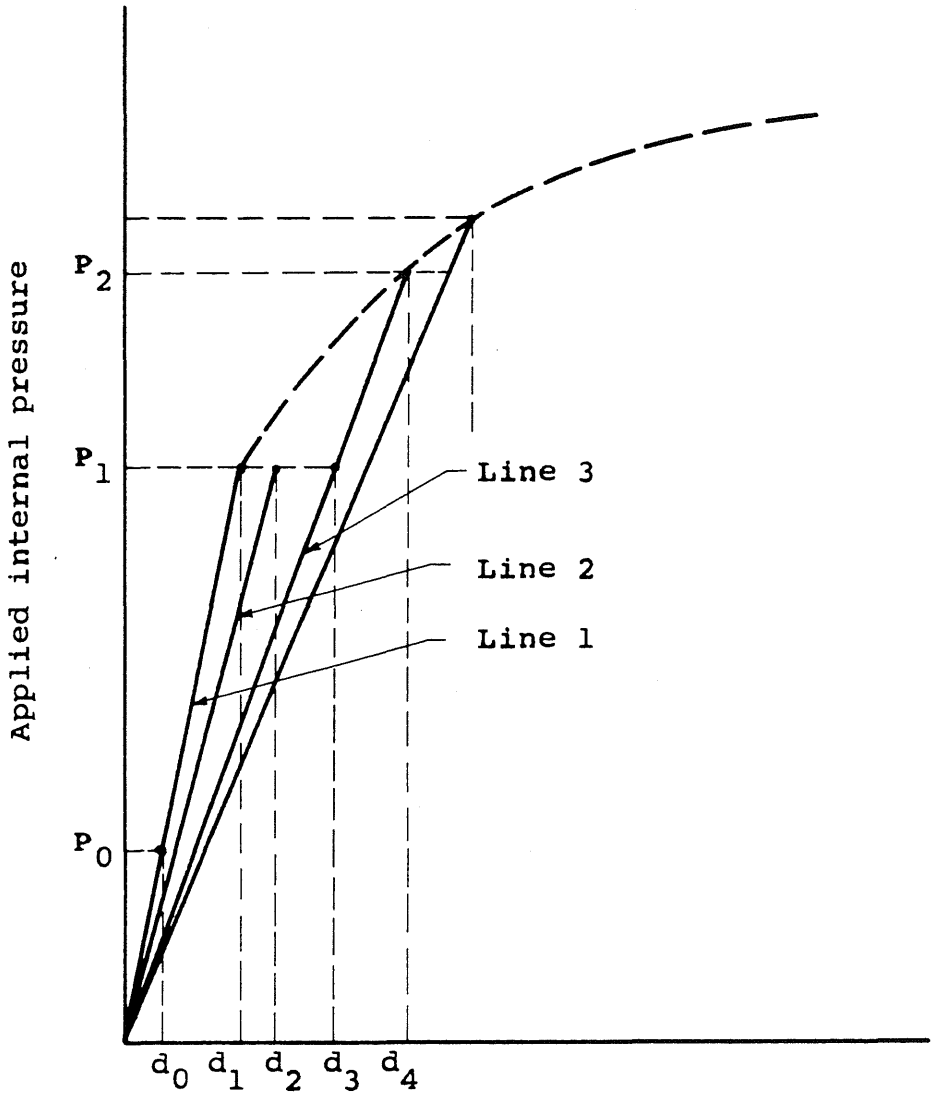

FIGURE 16. INCREMENTAL PROCESS

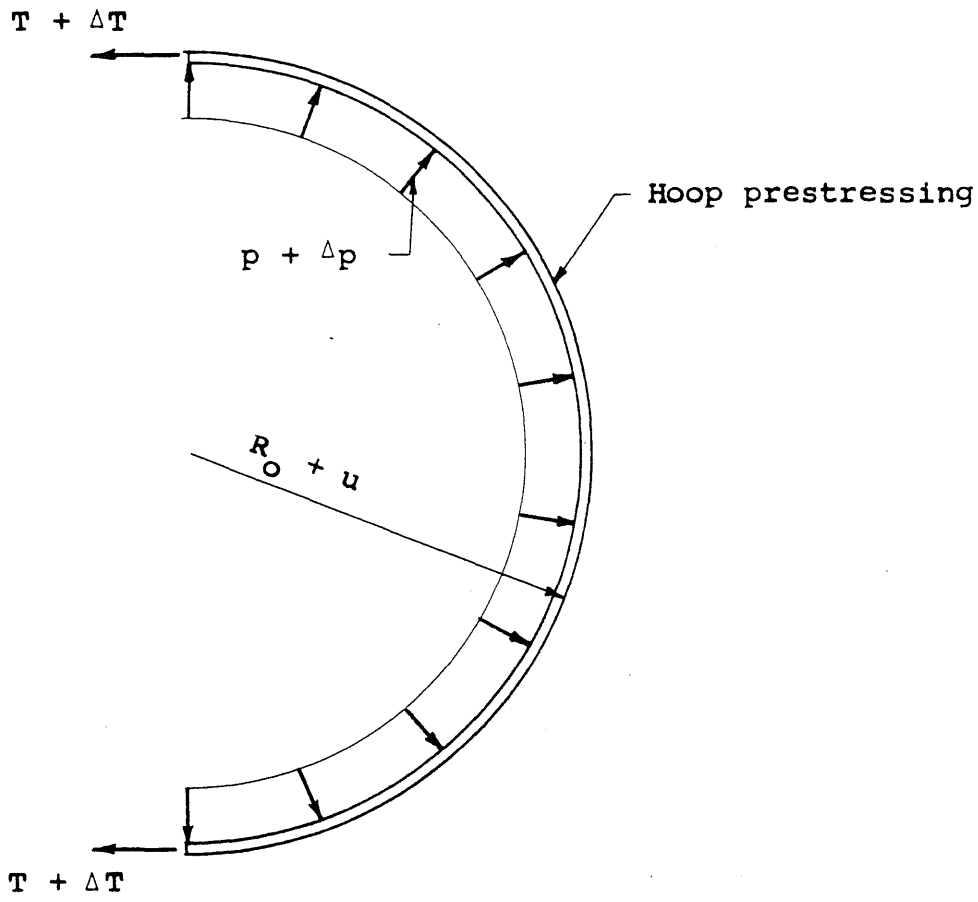

FIGURE 17. FORCES ACTING ON HOOP PRESTRESSING

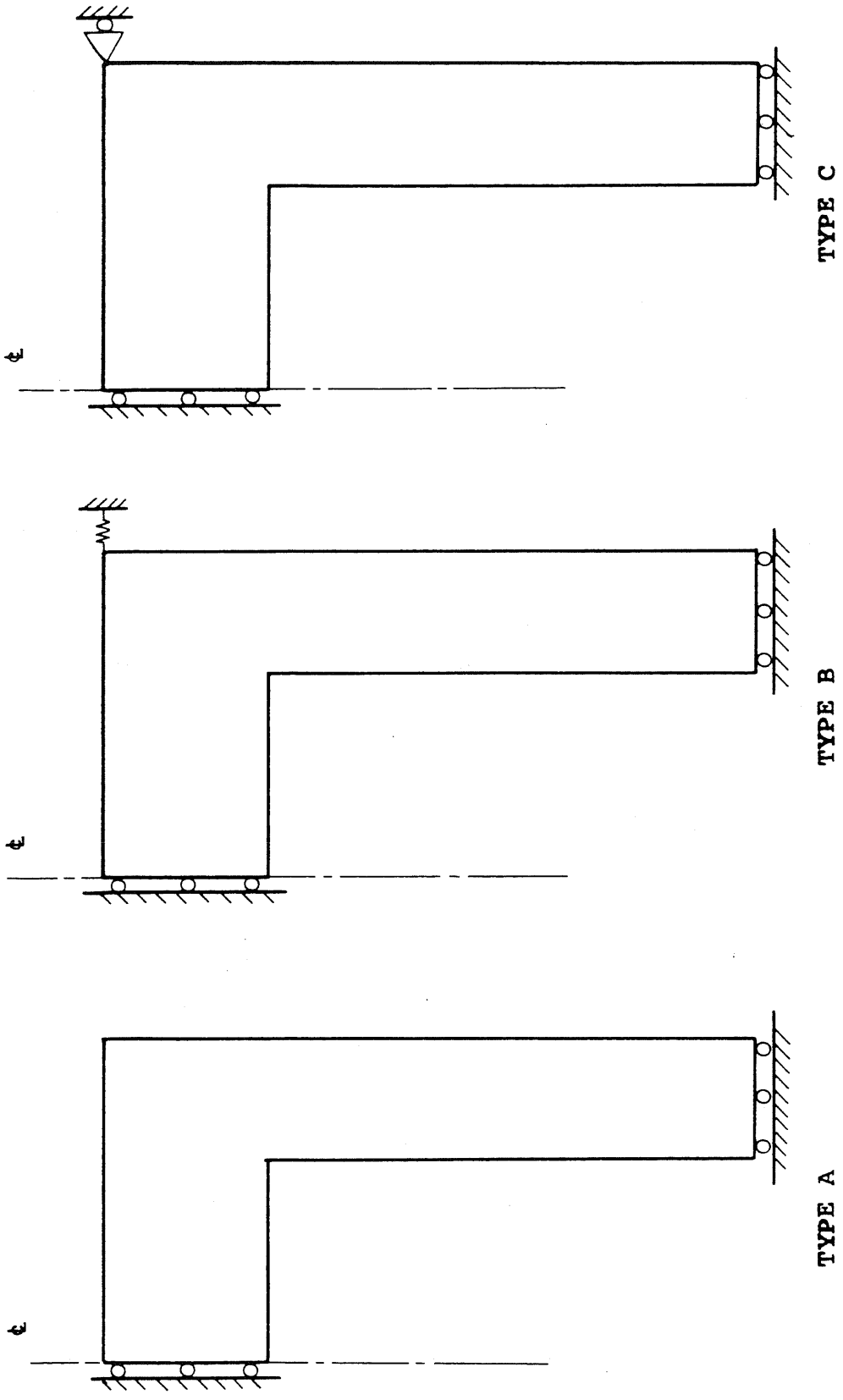

FIGURE 18. TYPES OF CONSTRAINT

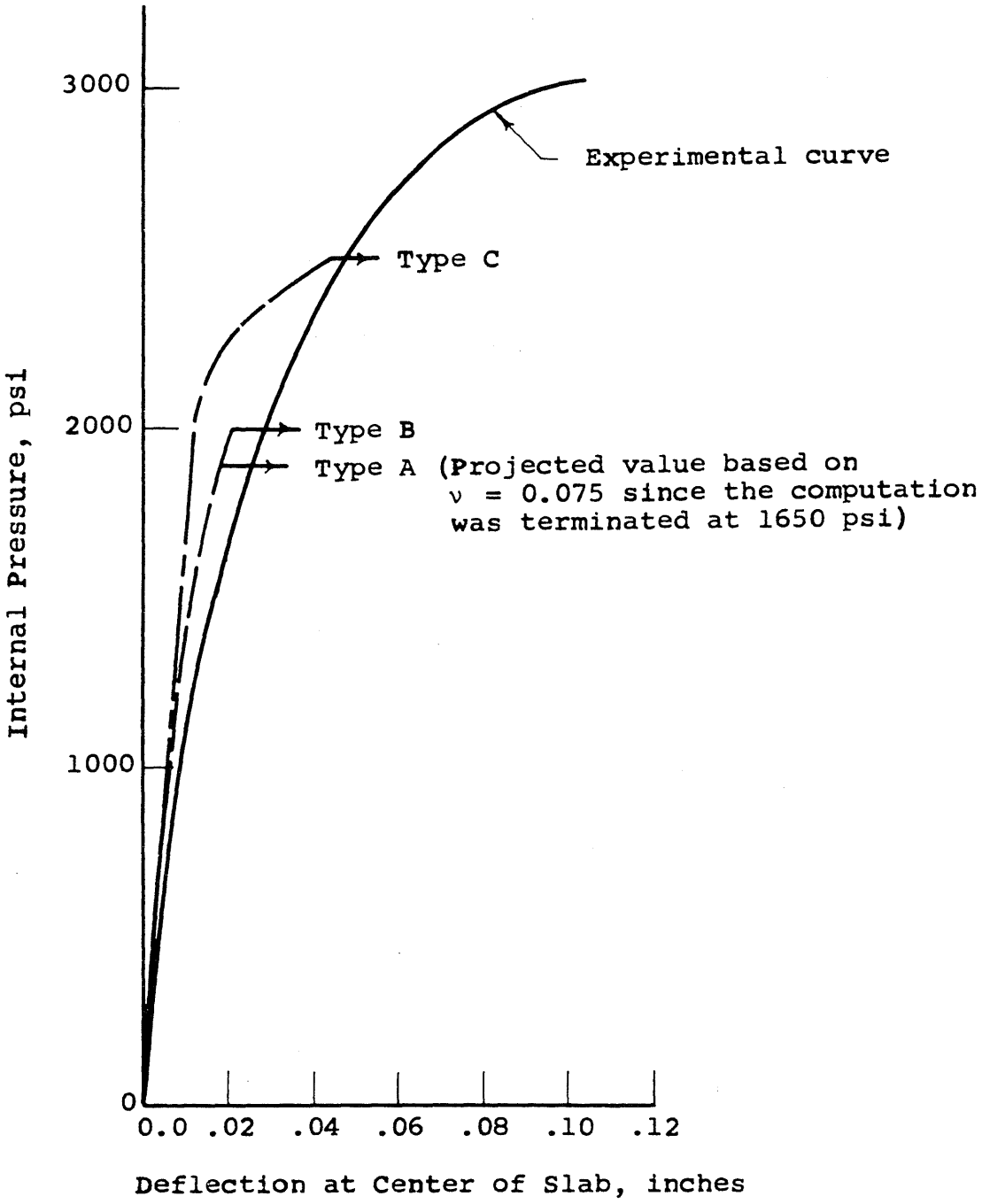

FIGURE 19. COMPARISON OF LOAD-DEFORMATION CURVES FOR $\nu = 0$

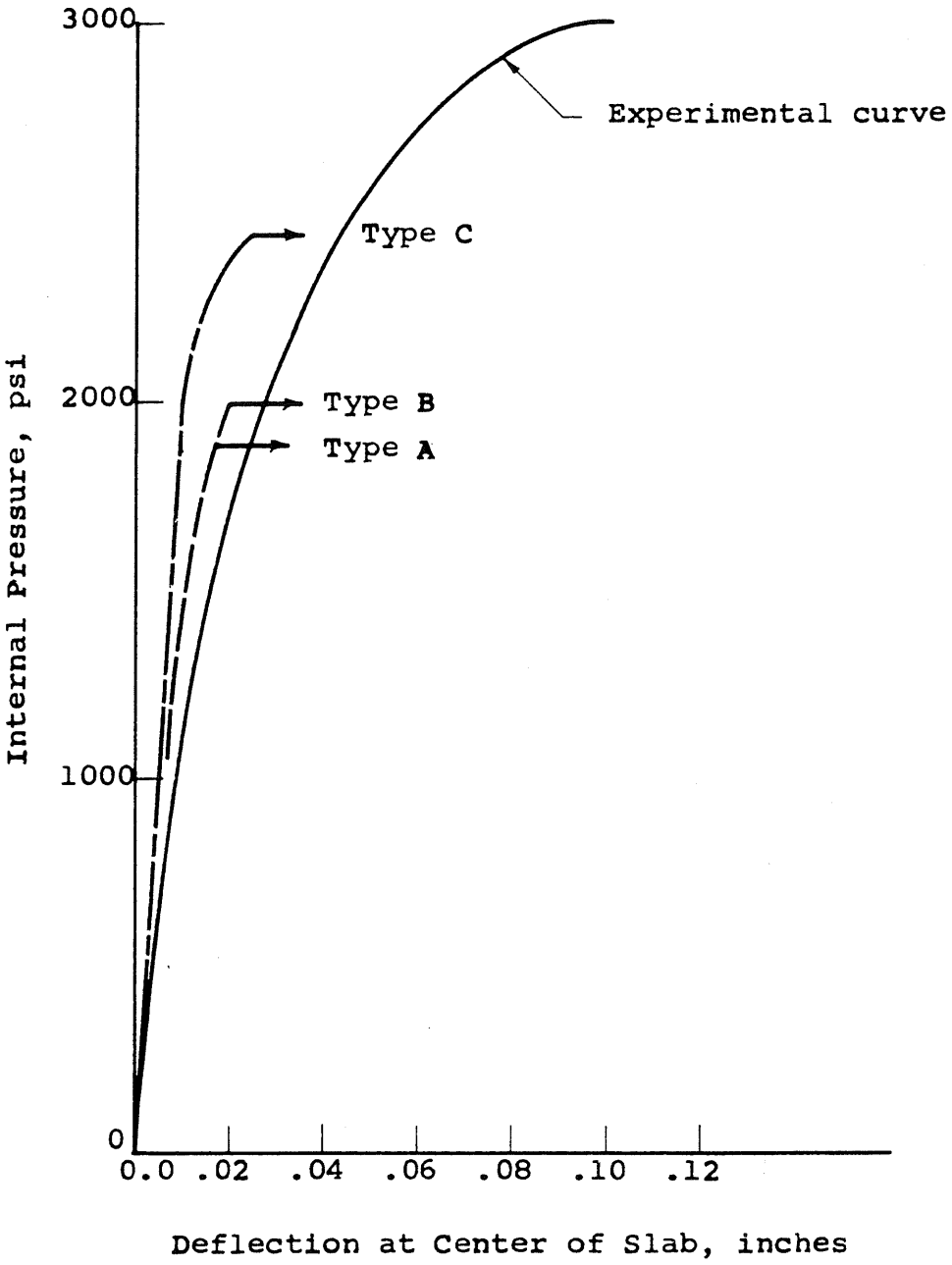

FIGURE 20. COMPARISON OF LOAD-DEFORMATION CURVES FOR $\nu = 0.075$

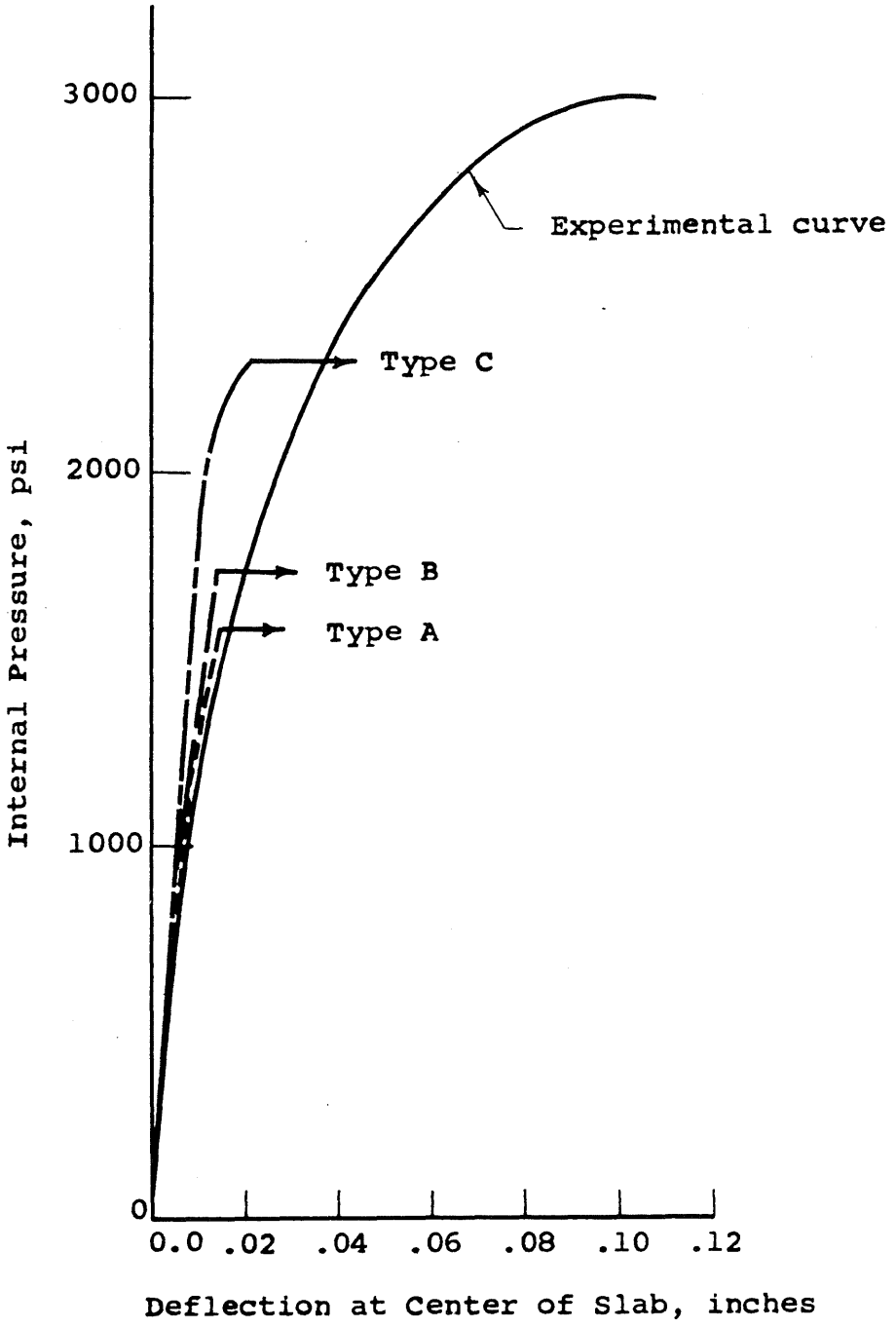

FIGURE 21. COMPARISON OF LOAD-DEFORMATION CURVES FOR $\nu = 0.15$

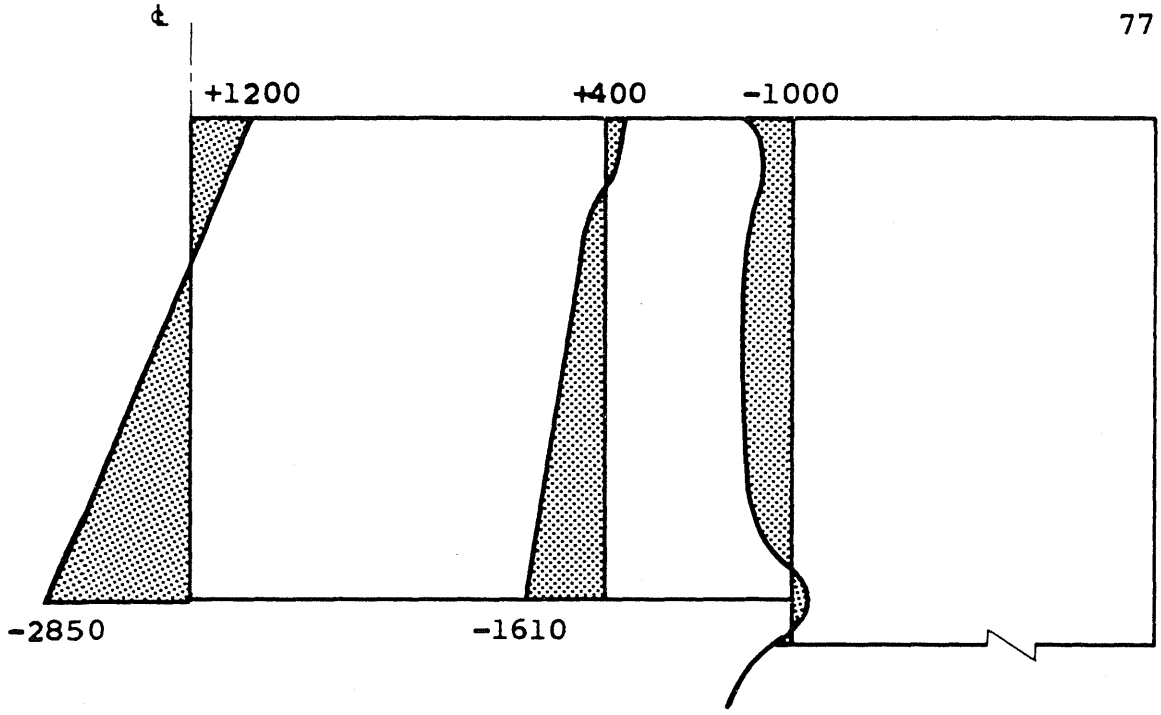

Prestressing + Internal Pressure of 1330 psi

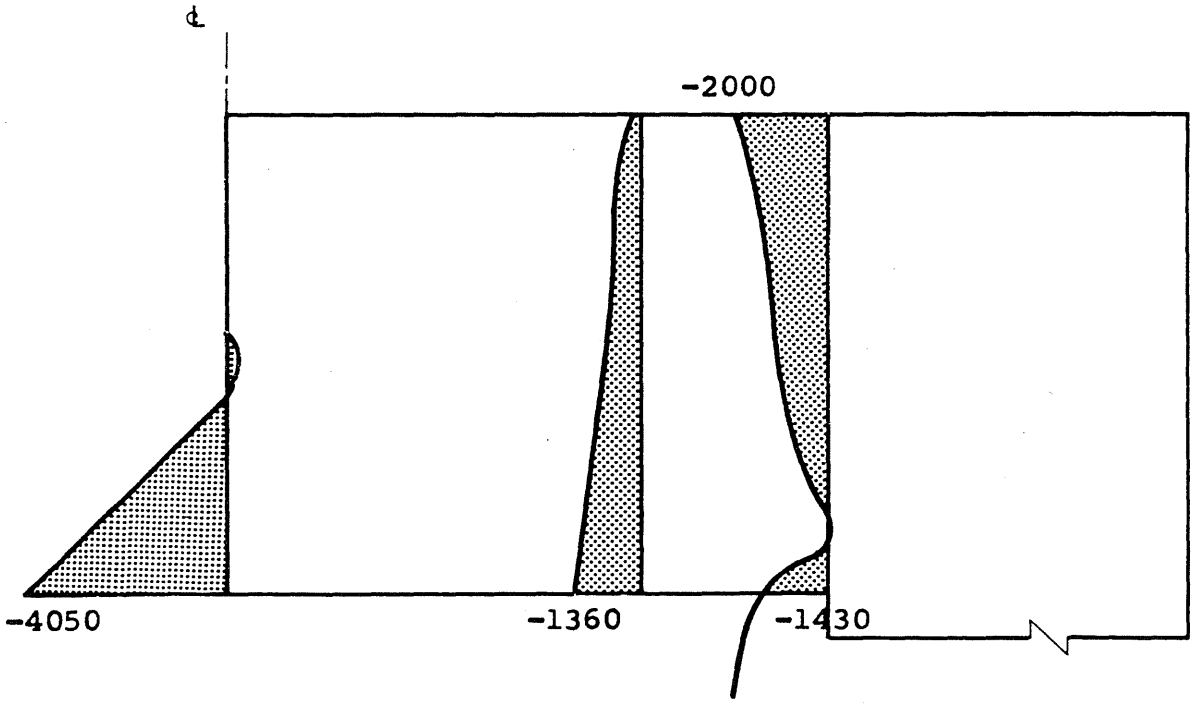

Prestressing + Internal Pressure of 2070 psi

FIGURE 22. RADIAL STRESSES (PSI) IN THE SLAB FOR TYPE B WITH $\nu = 0$

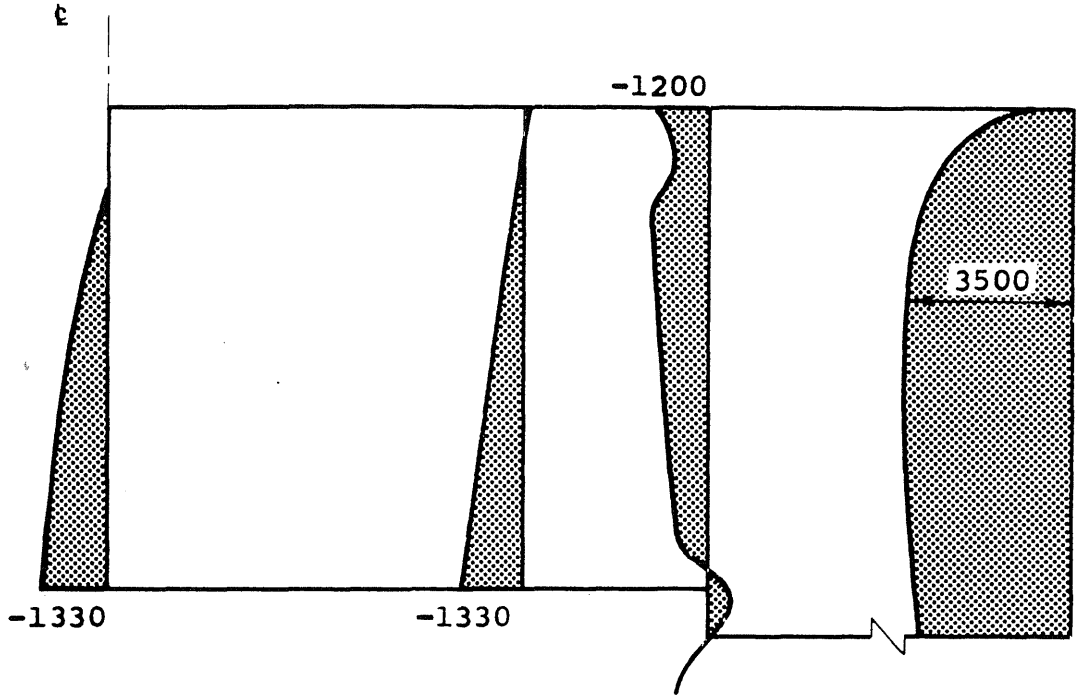

Prestressing + Internal Pressure of 1330 psi

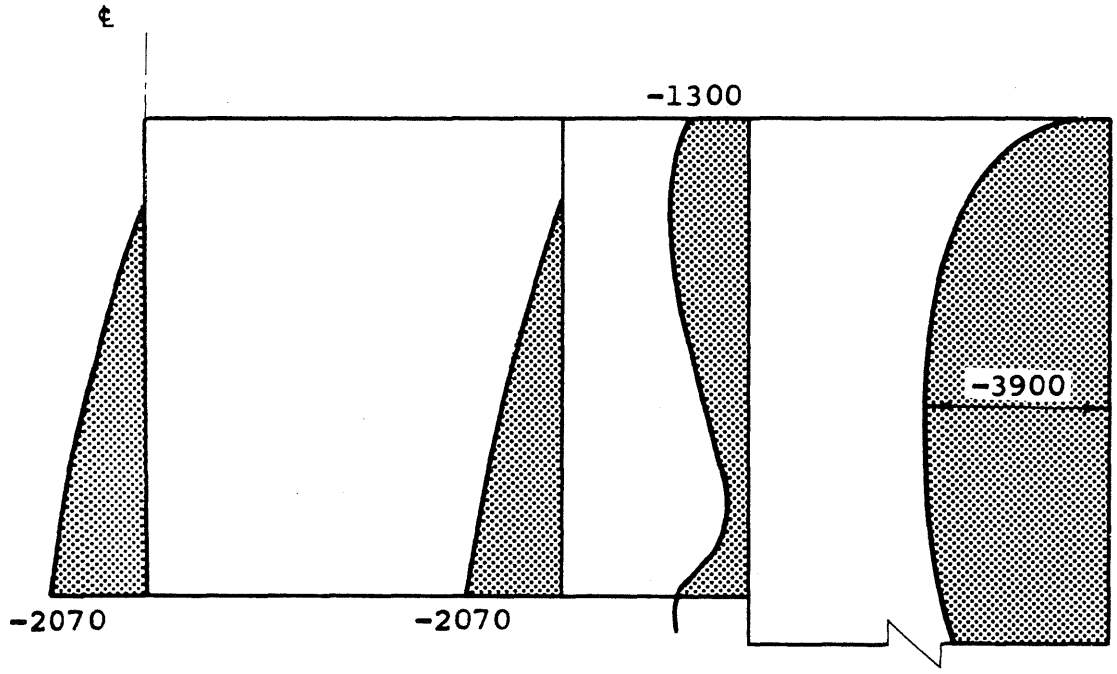

Prestressing + Internal Pressure of 2070 psi

FIGURE 23. VERTICAL STRESSES (PSI) IN THE SLAB FOR TYPE B WITH $\nu = 0$

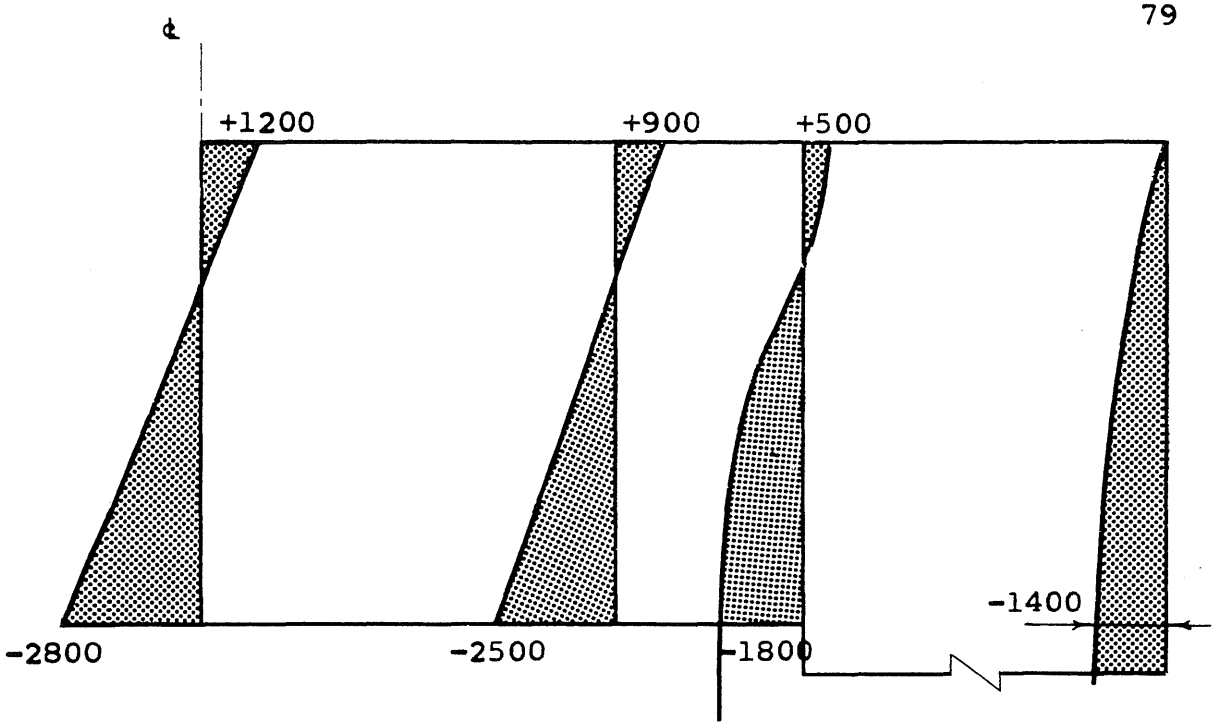

Prestressing + Internal Pressure of 1330 psi

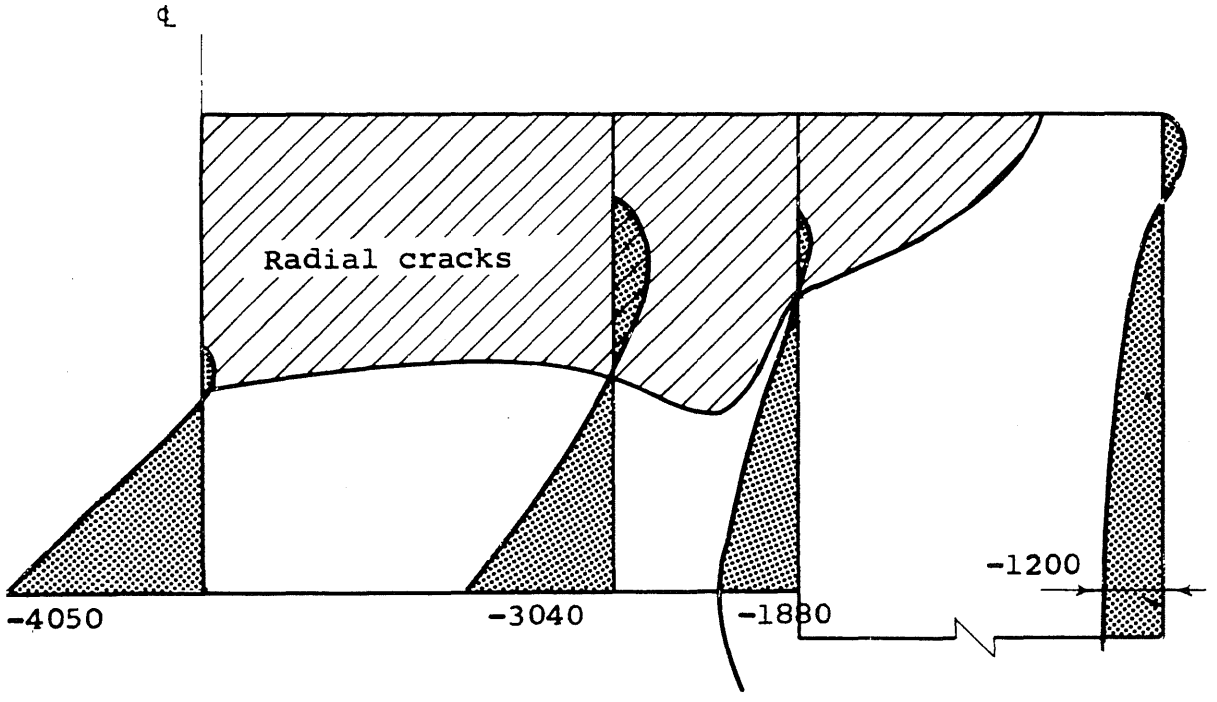

Prestressing + Internal Pressure of 2070 psi

FIGURE 24. CIRCUMFERENTIAL STRESSES (PSI) IN THE SLAB FOR TYPE B WITH $\nu = 0$

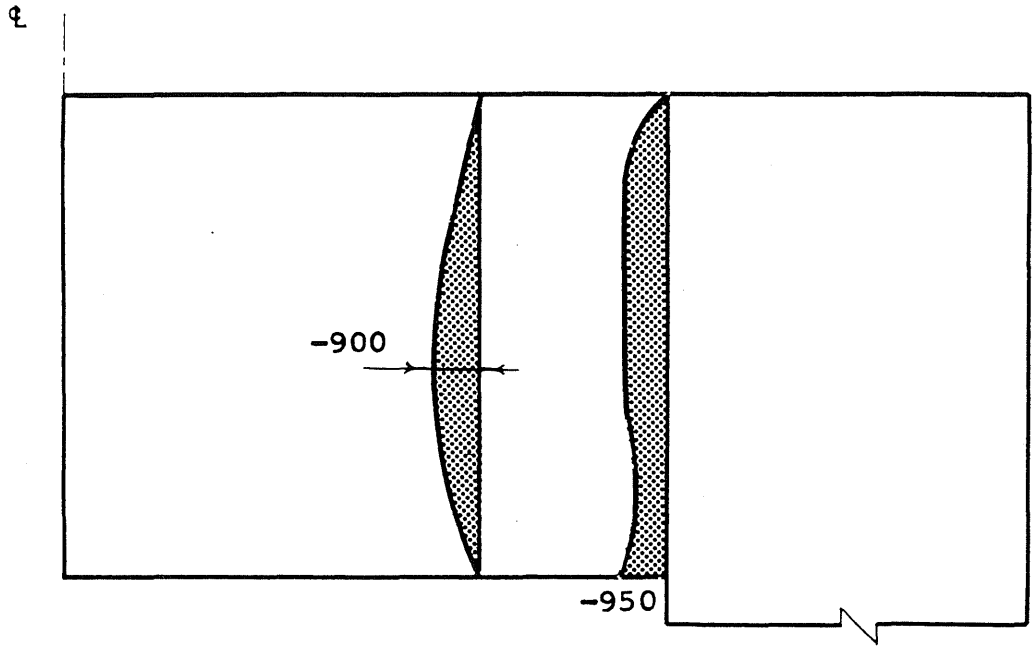

Prestressing + Internal Pressure of 1330 psi

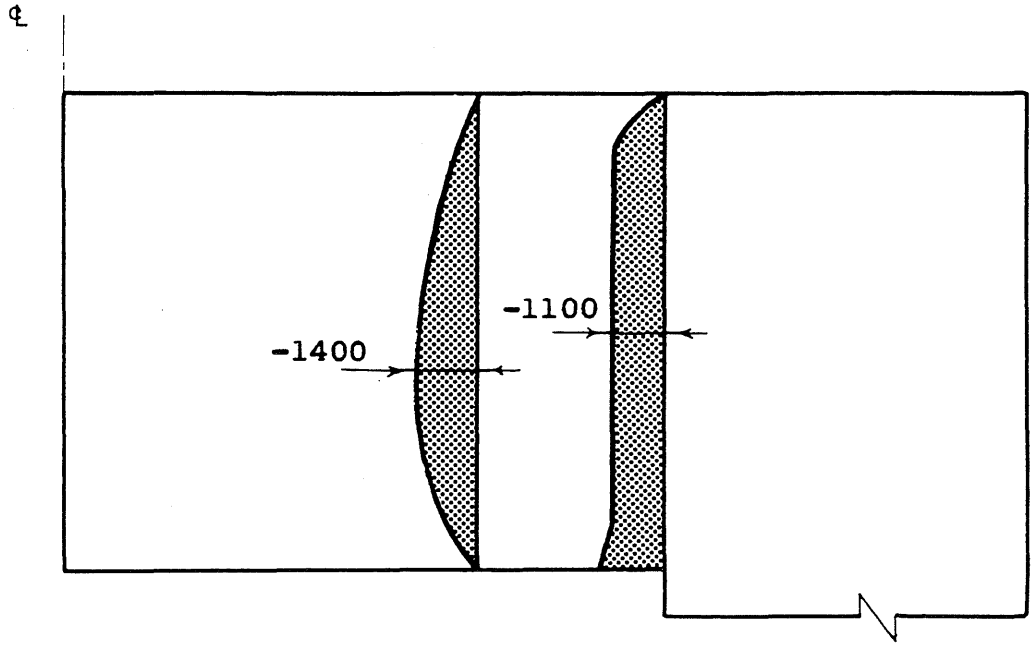

Prestressing + Internal Pressure of 2070 psi

FIGURE 25. SHEAR STRESSES (PSI) IN THE SLAB FOR TYPE B WITH $\nu = 0$

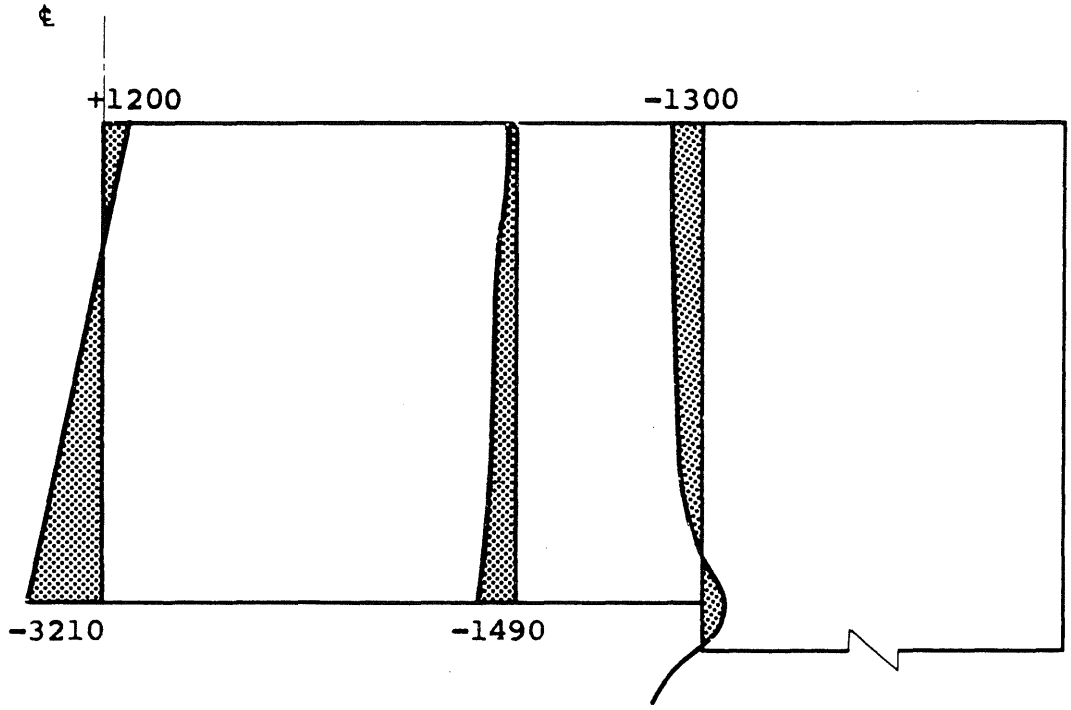

Prestressing + Internal Pressure of 2030 psi

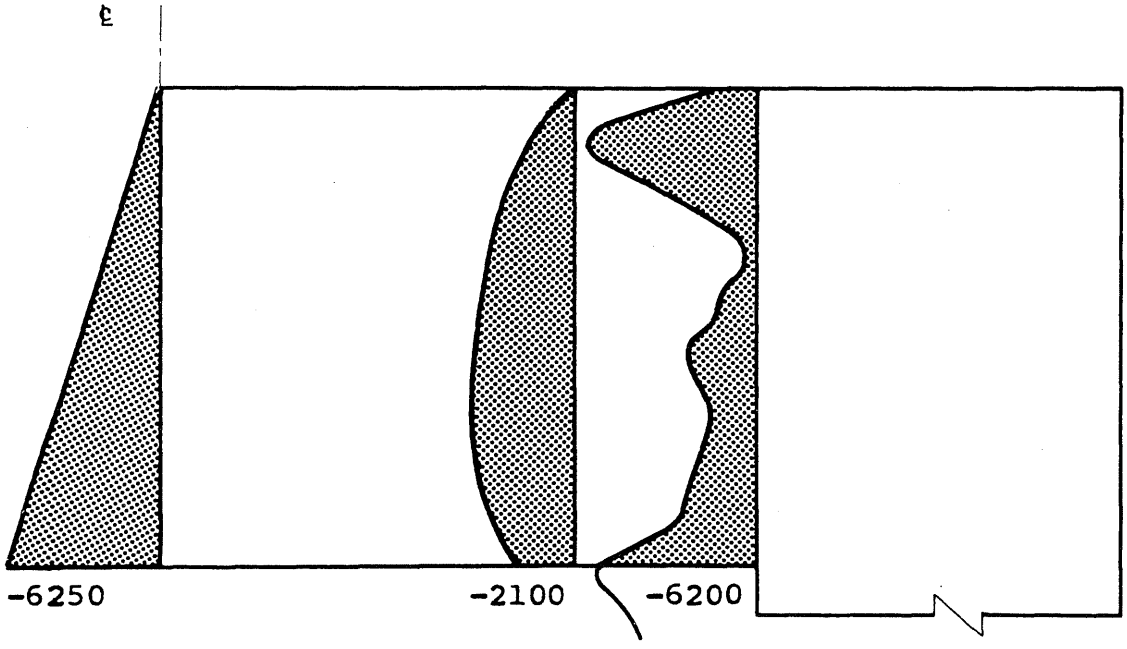

Prestressing + Internal Pressure of 2570 psi

FIGURE 26. RADIAL STRESSES (PSI) IN THE SLAB FOR TYPE C WITH $\nu = 0$

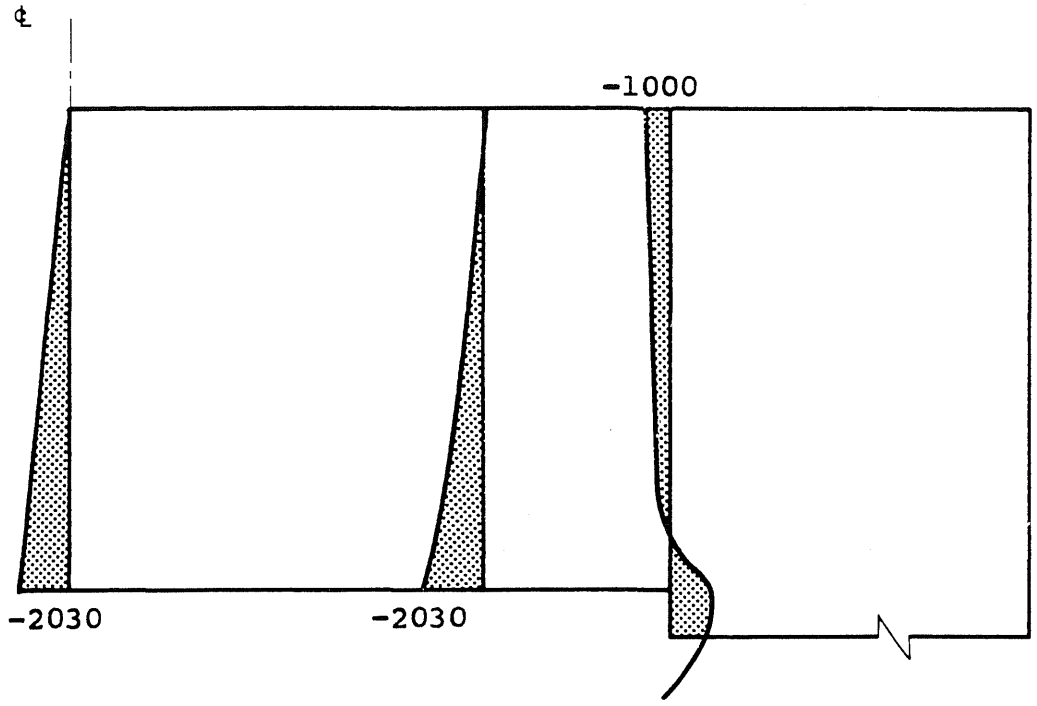

Prestressing + Internal Pressure of 2030 psi

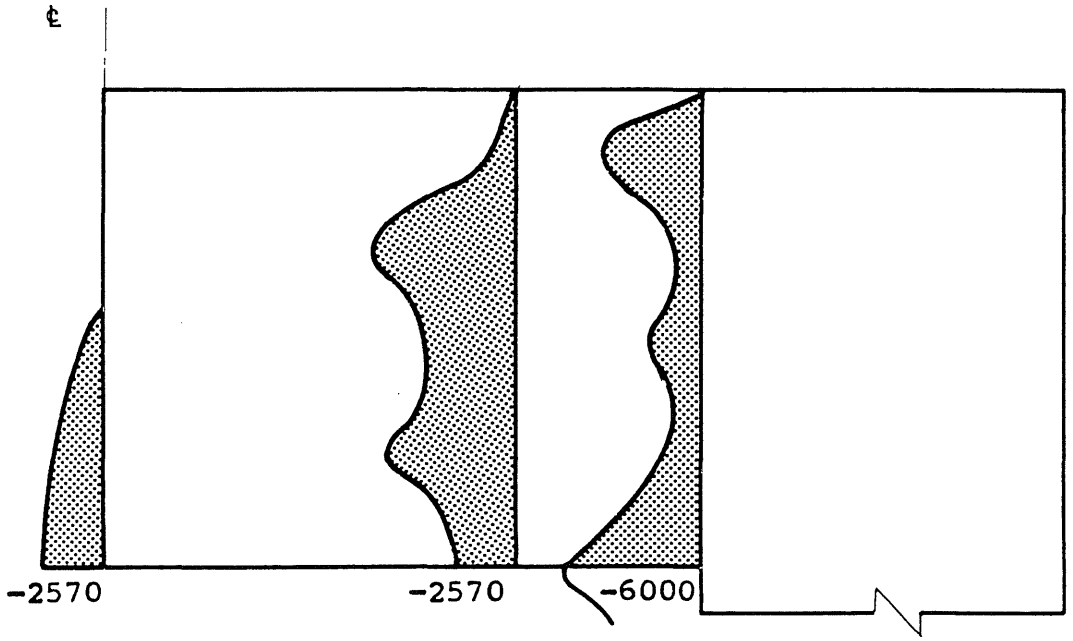

Prestressing + Internal Pressure of 2570 psi

FIGURE 27. VERTICAL STRESSES (PSI) IN THE SLAB FOR TYPE C WITH $\nu = 0$

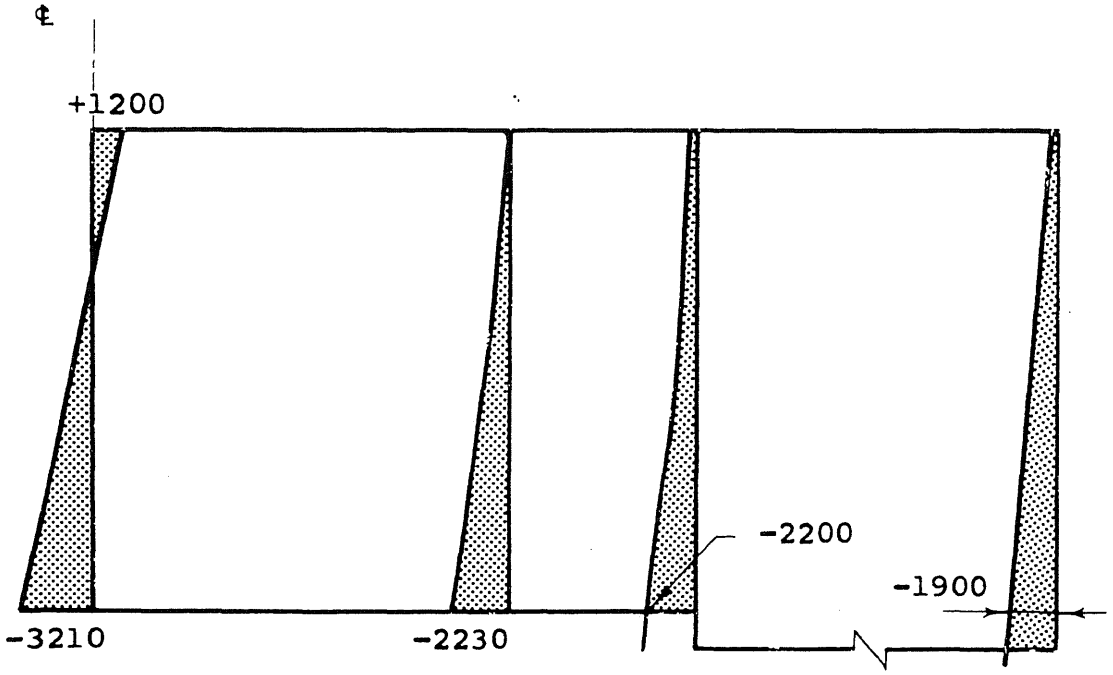

Prestressing + Internal Pressure of 2030 psi

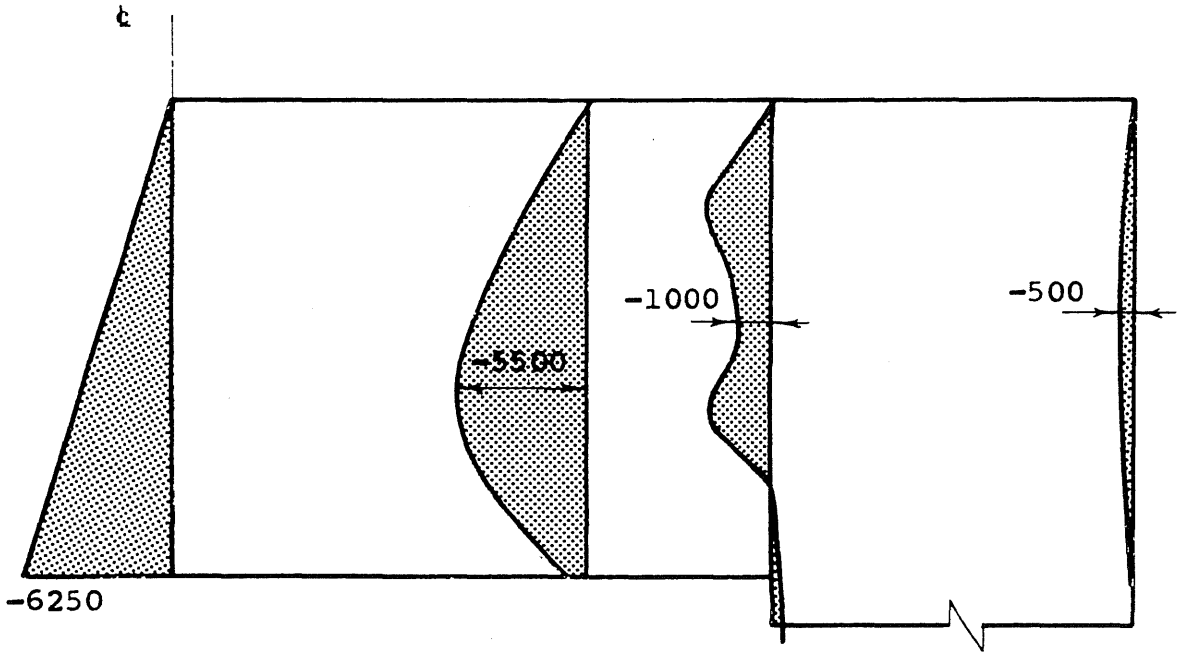

Prestressing + Internal Pressure of 2570 psi

FIGURE 28. CIRCUMFERENTIAL STRESSES (PSI) IN THE SLAB FOR TYPE C WITH $\nu = 0$

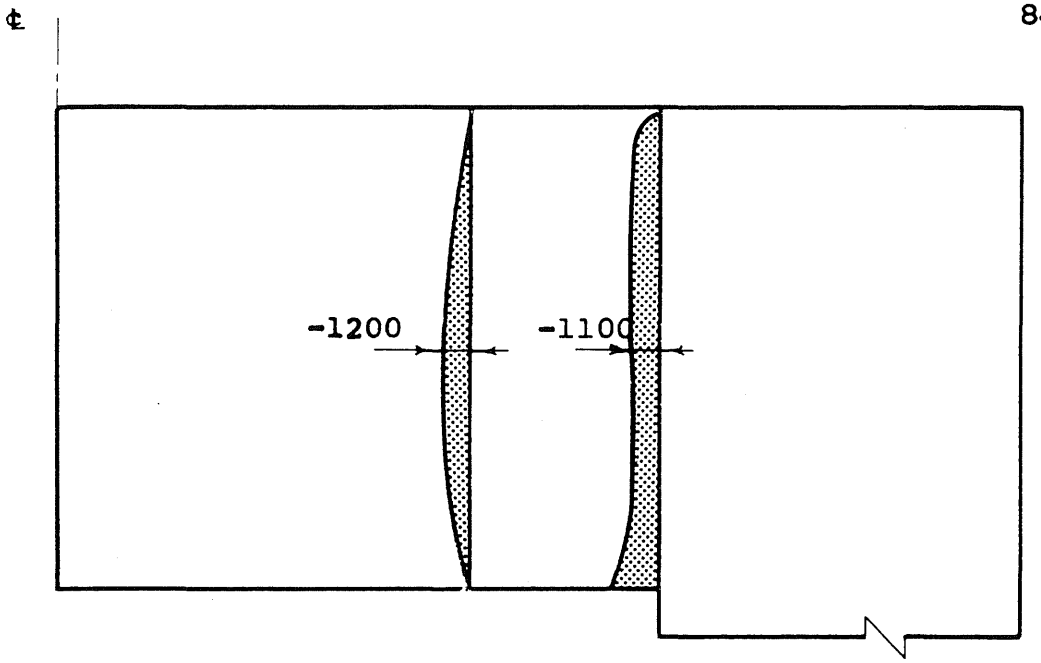

Prestressing + Internal Pressure of 2030 psi

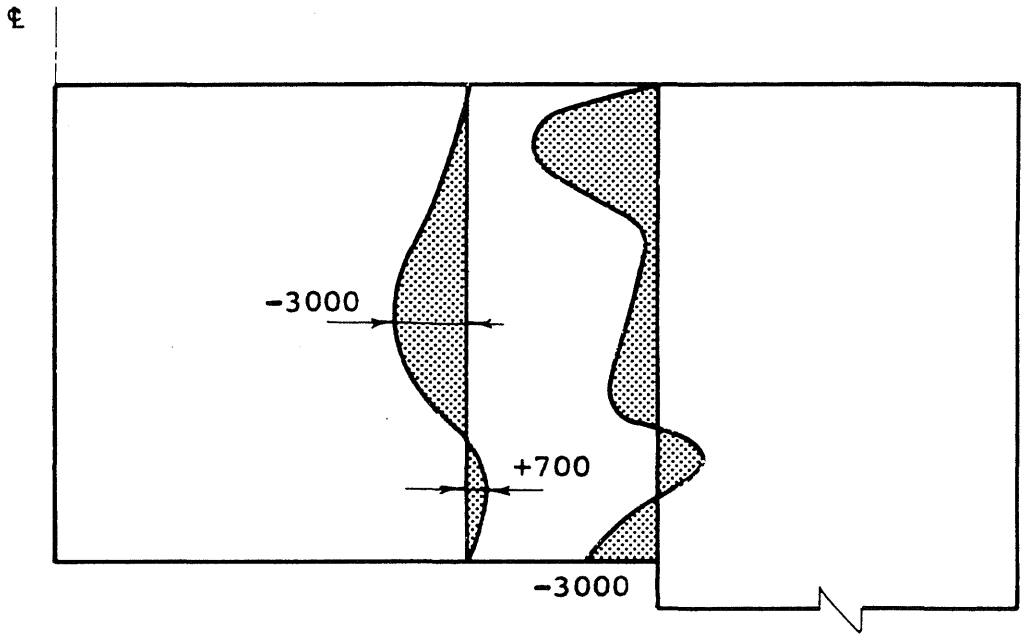

Prestressing + Internal Pressure of 2570 psi

FIGURE 29. SHEAR STRESSES (PSI) IN THE SLAB FOR TYPE C WITH $\nu = 0$

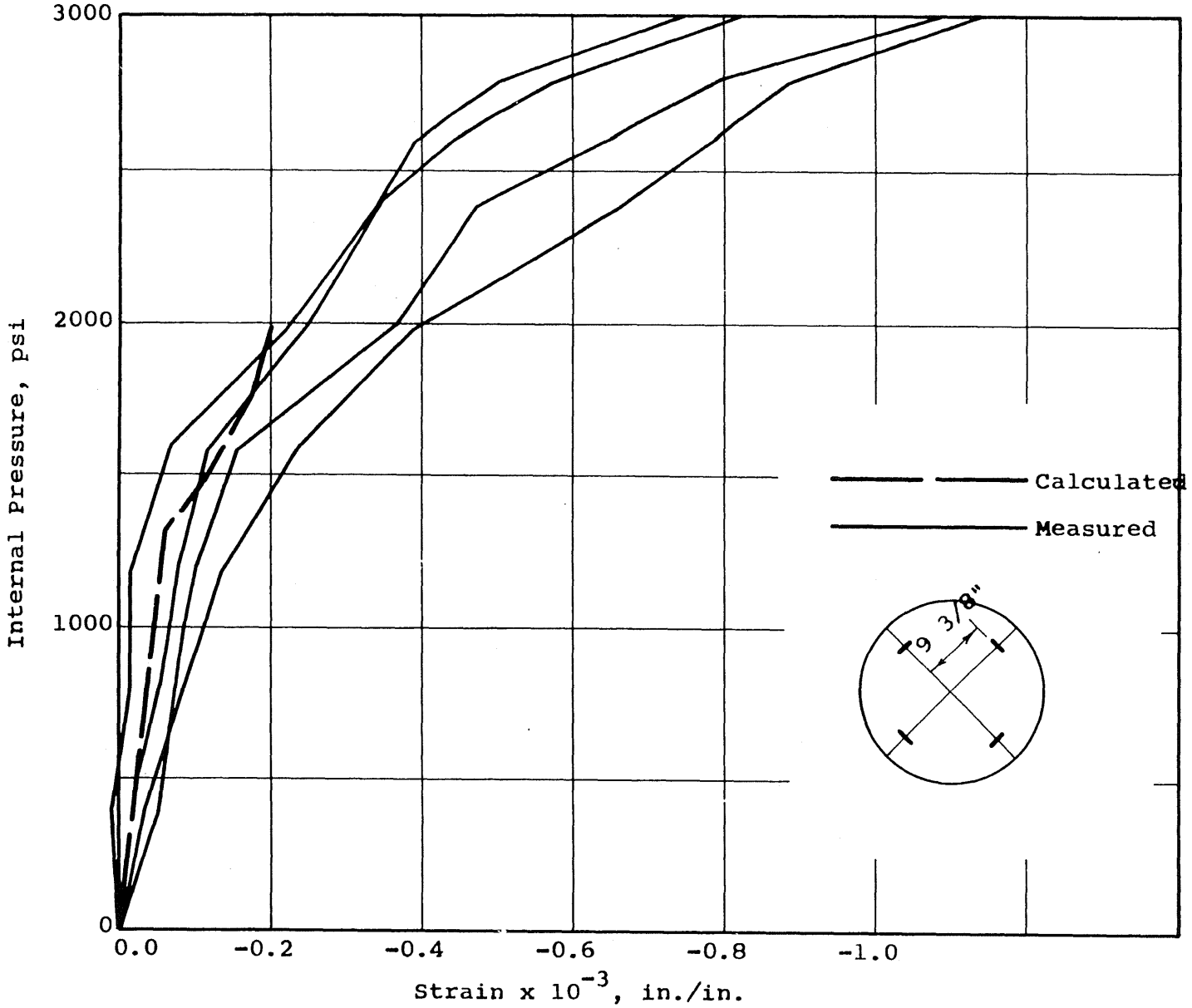

FIGURE 30. INTERNAL PRESSURE VS INSIDE CIRCUMFERENTIAL STRAIN AT RADIUS OF 9 3/8 INCHES

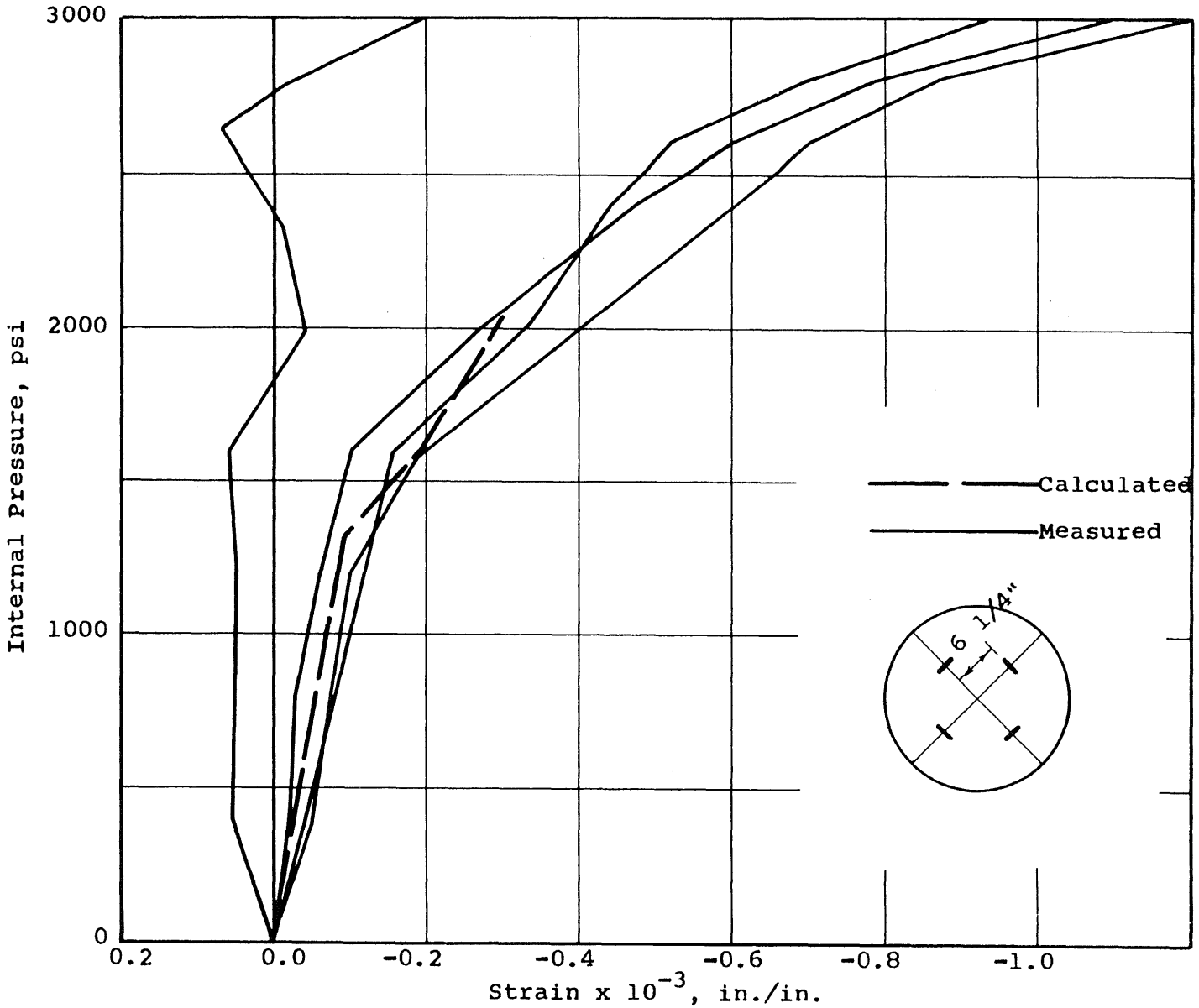

FIGURE 31. INTERNAL PRESSURE VS INSIDE CIRCUMFERENTIAL STRAIN AT RADIUS OF 6 1/4 INCHES

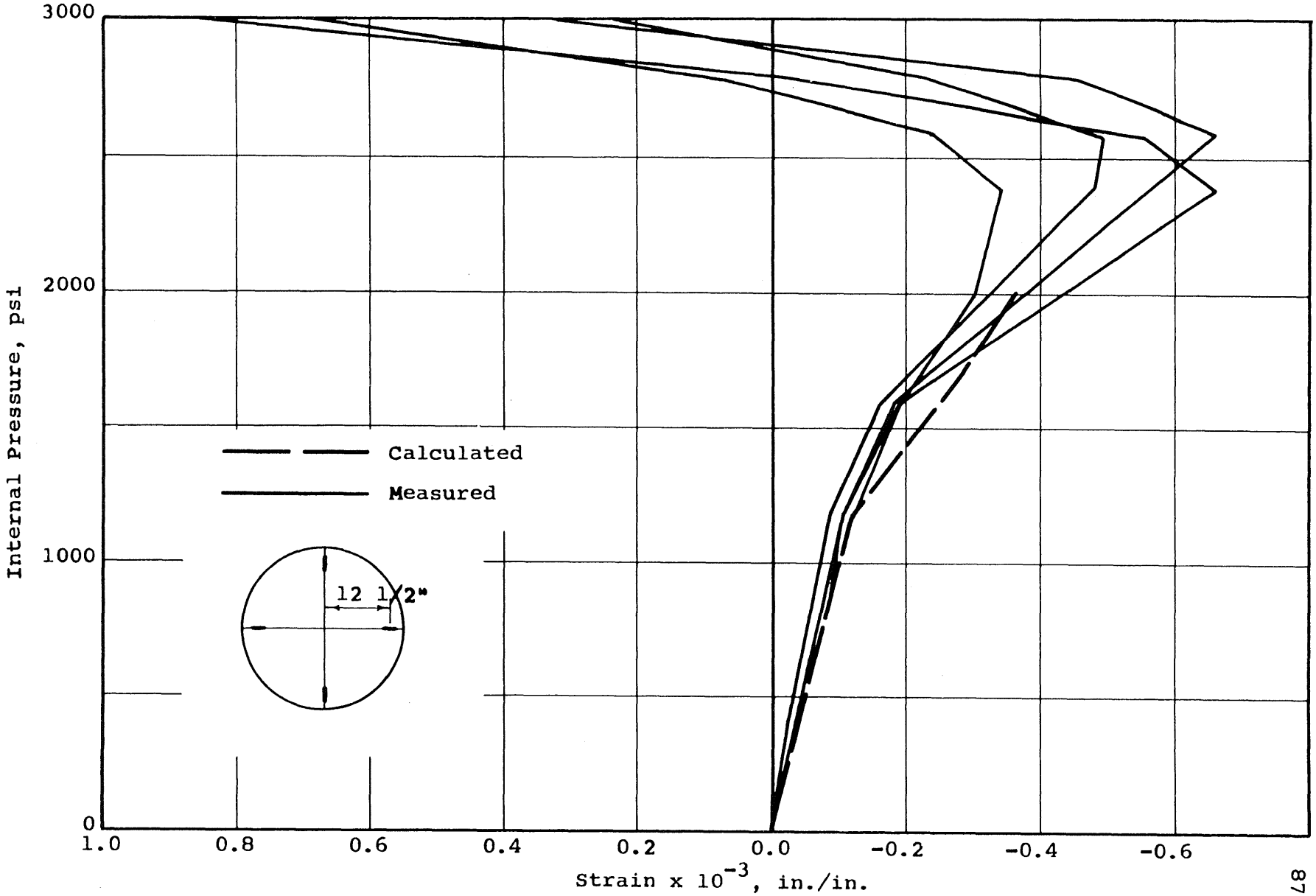

FIGURE 32. INTERNAL PRESSURE VS OUTSIDE RADIAL STRAIN AT RADIUS OF 12 1/2 INCHES

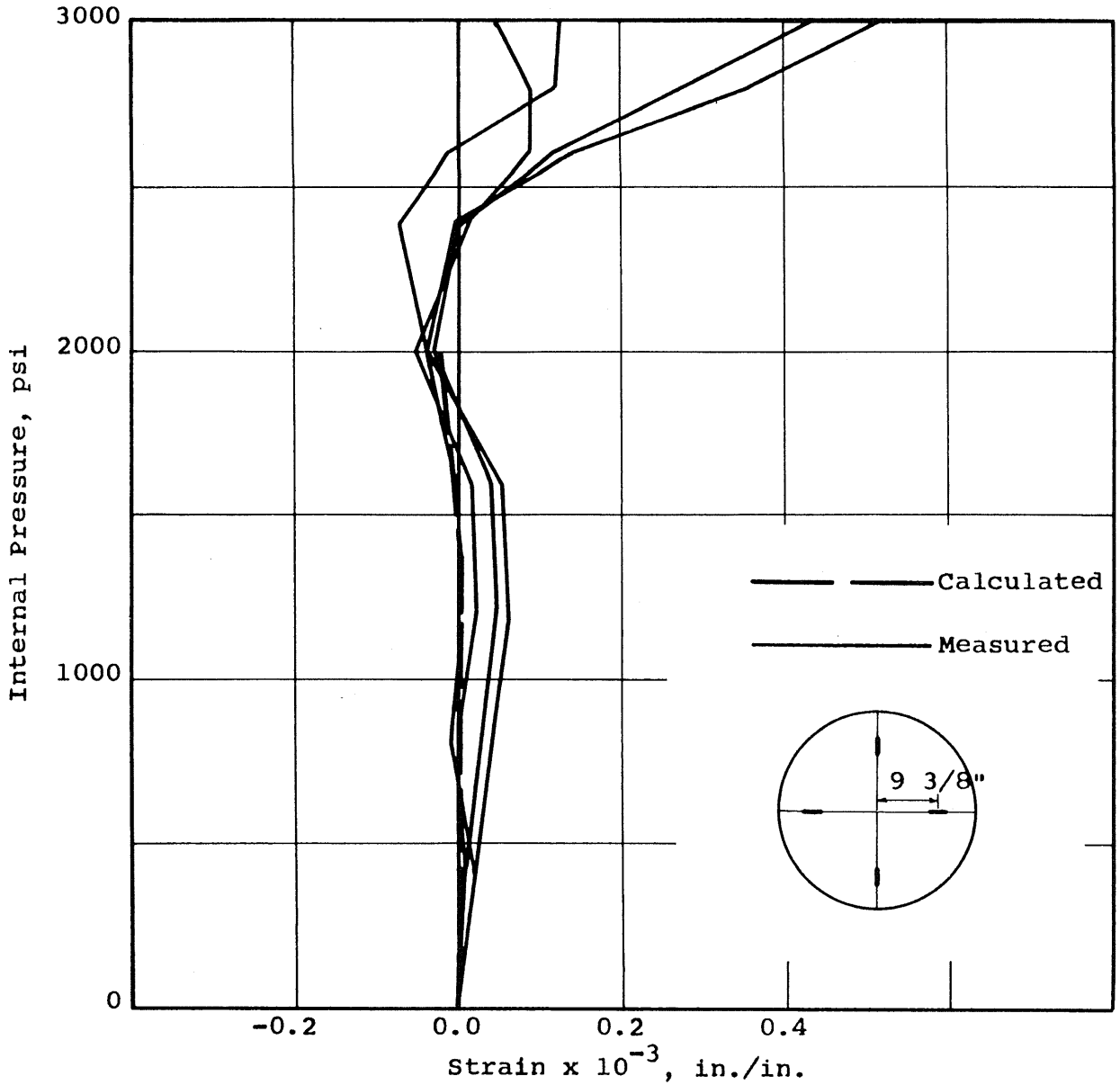

FIGURE 33. INTERNAL PRESSURE VS OUTSIDE RADIAL STRAIN AT RADIUS OF 9 3/8 INCHES

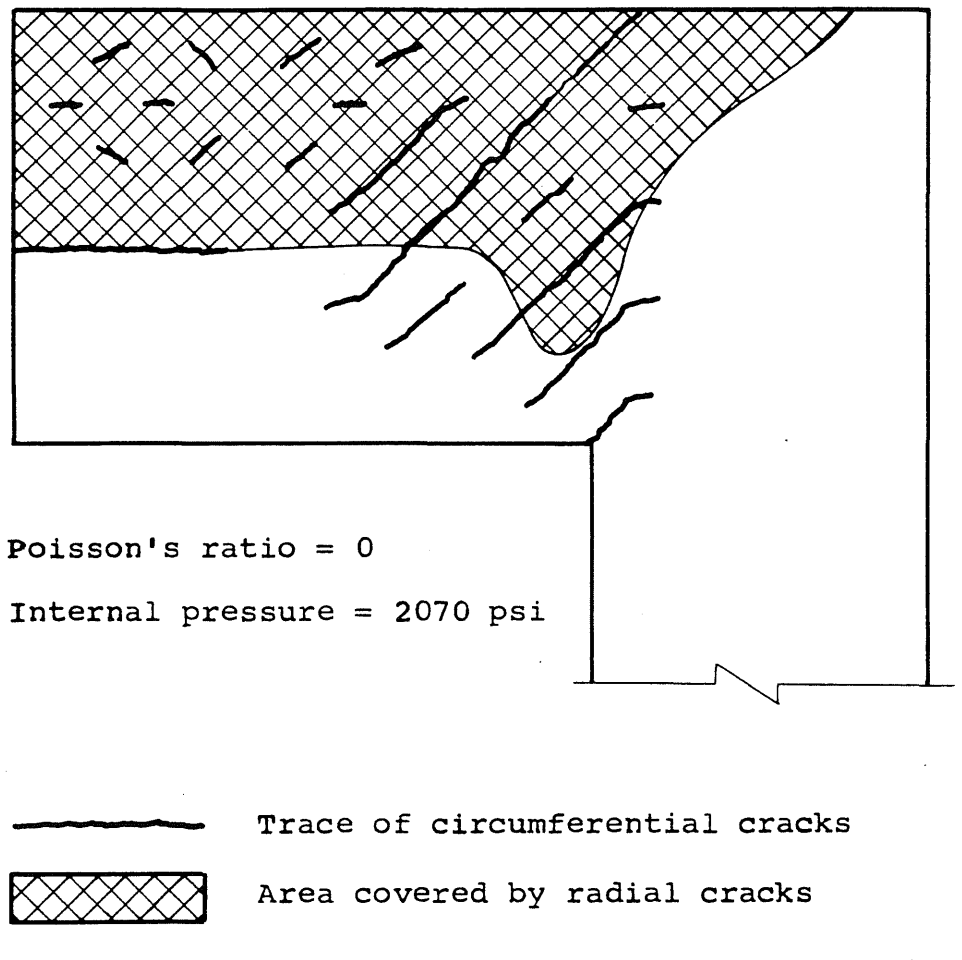

FIGURE 34. CRACK TRAJECTORIES FOR TYPE B CONSTRAINT

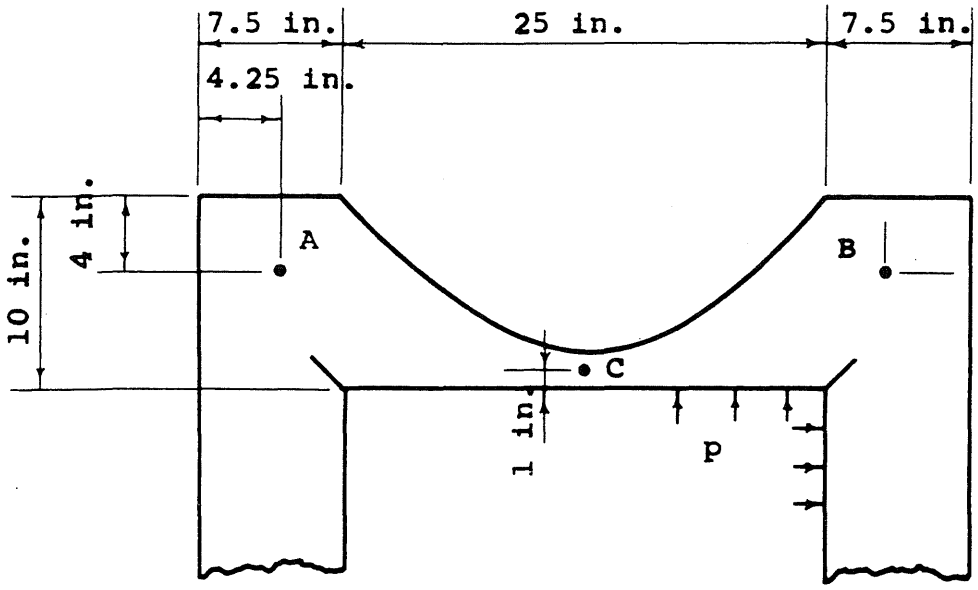

FIGURE 35a. AN IDEALIZED INVERTED DOME

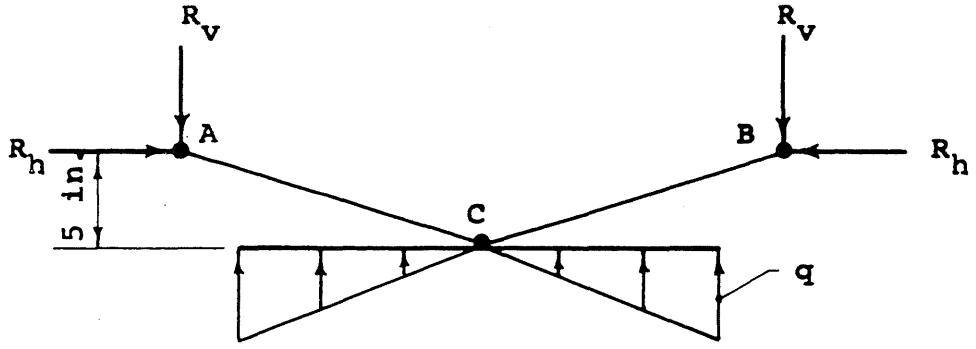

FIGURE 35b. A THREE-HINGED ARCH IDEALIZATION

APPENDIX

STIFFNESS OF ELEMENTS

General

The general element stiffness matrix for a lumped-parameter model is 8 by 8. The equilibrium equations for an element is:

$$V \begin{bmatrix} k_{11} & k_{12} & k_{13} & \cdot & \cdot & \cdot & \cdot & k_{18} \\ k_{21} & k_{22} & k_{23} & \cdot & \cdot & \cdot & \cdot & k_{28} \\ \cdot & \cdot & \cdot & \cdot & \cdot & \cdot & \cdot & \cdot \\ \cdot & \cdot & \cdot & \cdot & \cdot & \cdot & \cdot & \cdot \\ \cdot & \cdot & \cdot & \cdot & \cdot & \cdot & \cdot & \cdot \\ \cdot & \cdot & \cdot & \cdot & \cdot & \cdot & \cdot & \cdot \\ \cdot & \cdot & \cdot & \cdot & \cdot & \cdot & \cdot & \cdot \\ k_{81} & k_{82} & \cdot & \cdot & \cdot & \cdot & \cdot & k_{88} \end{bmatrix} \begin{Bmatrix} u_1 \\ v_1 \\ u_2 \\ v_2 \\ u_3 \\ v_3 \\ u_4 \\ v_4 \end{Bmatrix} = \begin{Bmatrix} P_{r1} \\ P_{z1} \\ P_{r2} \\ P_{z2} \\ P_{r3} \\ P_{v3} \\ P_{r4} \\ P_{z4} \end{Bmatrix}$$

The symbol V in above formulation stands for the volume of an element.

Typical Interior Element

$$V = \pi R L_r L_z$$

$$k_{11} = C_{44}/L_z^2, \qquad k_{12} = C_{42}/L_z^2,$$

$$k_{13} = C_{14}/(L_r L_z) - C_{43}/(2 R L_z),$$

$$k_{14} = C_{44}/(L_r\ L_z), \qquad k_{15} = -\,k_{11}, \qquad k_{16} = -\,k_{12},$$

$$k_{17} = -\,C_{41}/(L_r\ L_z) - C_{43}/(2\ R\ L_z),$$

$$k_{18} = -\,k_{14},$$

$$k_{21} = C_{24}/L_z^{\,2}, \qquad k_{22} = C_{22}/L_z^{\,2},$$

$$k_{23} = C_{21}/(L_r\ L_z) - C_{23}/(2\ R\ L_z),$$

$$k_{24} = C_{24}/(L_r\ L_z), \qquad k_{25} = -\,k_{21}, \qquad k_{26} = -\,k_{22},$$

$$k_{27} = -\,C_{21}/(L_r\ L_z) - C_{23}/(2\ R\ L_z), \qquad k_{28} = -\,k_{24},$$

$$k_{31} = C_{14}/(L_r\ L_z) - C_{34}/(2\ R\ L_z),$$

$$k_{32} = C_{12}/(L_r\ L_z) - C_{32}/(2\ R\ L_z),$$

$$k_{33} = C_{11}/L_r^{\,2} - C_{31}/(2\ R\ L_r) - C_{13}/(2\ R\ L_r) + C_{33}/(4\ R^2),$$

$$k_{34} = C_{14}/L_r^{\,2} - C_{34}/(2\ R\ L_r), \qquad k_{35} = -\,k_{31},$$

$$k_{36} = -\,k_{32},$$

$$k_{37} = -\,C_{11}/L_r^{\,2} + C_{31}/(2\ R\ L_r) - C_{13}/(2\ R\ L_r) + C_{33}/(4R^2),$$

$$k_{38} = -\,k_{34},$$

$$k_{41} = C_{44}/(L_r\ L_z), \qquad k_{42} = C_{42}/(L_r\ L_z),$$

$$k_{43} = C_{41}/L_r^{\,2} - C_{43}/(2\ R\ L_r), \qquad k_{44} = C_{44}/L_r^{\,2},$$

$$k_{45} = -\,k_{41}, \qquad k_{46} = -\,k_{42},$$

$$k_{47} = -\,C_{41}/L_r^{\,2} - C_{43}/(2\ R\ L_r), \qquad k_{48} = -\,k_{44},$$

$$k_{51} = -\,k_{11}, \qquad k_{52} = -\,k_{12}, \qquad k_{53} = -\,k_{13},$$

$$k_{54} = -\,k_{14}, \qquad k_{55} = -\,k_{15}, \qquad k_{56} = -\,k_{16},$$

$$k_{57} = - k_{17}, \qquad k_{58} = - k_{18},$$

$$k_{61} = - k_{21}, \qquad k_{62} = - k_{22}, \qquad k_{63} = - k_{23},$$

$$k_{64} = - k_{24}, \qquad k_{65} = - k_{25}, \qquad k_{66} = - k_{26},$$

$$k_{67} = - k_{27}, \qquad k_{68} = - k_{28},$$

$$k_{71} = - C_{14}/(L_r\ L_z) - C_{34}/(2\ R\ L_z),$$

$$k_{72} = - C_{12}/(L_r\ L_z) - C_{32}/(2\ R\ L_z),$$

$$k_{73} = - C_{11}/L_r^2 - C_{31}/(2\ R\ L_r) + C_{13}/(2\ R\ L_r) + C_{33}/(4R^2),$$

$$k_{74} = - C_{14}/L_r^2 - C_{34}/(2\ R\ L_r), \qquad k_{75} = - k_{71},$$

$$k_{76} = - k_{72},$$

$$k_{77} = C_{11}/L_r^2 + C_{31}/(2\ R\ L_2) + C_{13}/(2\ R\ L_r) + C_{33}/(4R^2),$$

$$k_{78} = - k_{74},$$

$$k_{81} = - k_{41}, \qquad k_{82} = - k_{42}, \qquad k_{83} = - k_{43},$$

$$k_{84} = - k_{44}, \qquad k_{85} = - k_{45}, \qquad k_{86} = - k_{46},$$

$$k_{87} = - k_{47}, \qquad k_{88} = - k_{48}$$

Along Vertical Axis of Symmetry

$$V = L_r\ L_z^2/12$$

$$k_{22} = C_{22}/L_z^2, \qquad k_{26} = - k_{22},$$

$$k_{27} = - 2(C_{21} + C_{23})/(L_r\ L_z),$$

$$k_{62} = - k_{22}, \qquad k_{66} = k_{22},$$

$$k_{67} = 2(C_{21} + C_{23})/(L_r\ L_z),$$

$$k_{72} = -\ 2(C_{12} + C_{32})/(L_r\ L_z), \qquad k_{76} = -\ k_{72},$$

$$k_{77} = 4(C_{11} + C_{31} + C_{13} + C_{33})/L_r^{\,2}$$

All other elements of the stiffness matrix are zero.

Along Top and Bottom of Slab

$$V = 0.5\ \pi\ R\ L_r\ L_z$$

$$k_{33} = C_{11}/L_r^{\,2} - C_{31}/(2\ R\ L_r) - C_{13}/(2\ R\ L_r) + C_{33}/(4R^2),$$

$$k_{37} = -\ C_{11}/L_r^{\,2} + C_{31}/(2\ R\ L_r) - C_{13}/(2\ R\ L_r) + C_{33}/(4R^2),$$

$$k_{73} = -\ C_{11}/L_r^{\,2} - C_{31}/(2\ R\ L_r) + C_{13}/(2\ R\ L_r) + C_{33}/(4R^2),$$

$$k_{77} = C_{11}/L_r^{\,2} + C_{31}/(2\ R\ L_r) + C_{13}/(2\ R\ L_r) + C_{33}/(4R^2)$$

All other elements of the stiffness matrix are zero.

Along Exterior and Interior of Wall

At exterior wall: $V = \pi\ L_r\ L_z\ (R - L_r/6)/2$

At interior wall: $V = \pi\ L_r\ L_z\ (R + L_r/3)/2$

$$k_{22} = C_{22}/L_z^{\,2}, \qquad k_{23} = -\ C_{23}/(R\ L_z), \qquad k_{26} = -\ k_{22},$$

$$k_{32} = -\ C_{32}/(R\ L_z), \qquad k_{33} = C_{33}/R^2, \qquad k_{36} = -\ k_{32},$$

$$k_{62} = -\ k_{22}, \qquad k_{63} = -\ k_{23}, \qquad k_{66} = k_{22}$$

All other elements of stiffness matrix are zero.

Along Horizontal Axis of Symmetry

$$V = 0.5\ R\ L_r\ L_z$$

$$k_{33} = C_{11}/L_r^2 - C_{31}/(2\ R\ L_r) - C_{13}/(2\ R\ L_r) + C_{33}/(4R^2),$$

$$k_{36} = -\ 2\ C_{12}/(L_r\ L_z) + C_{32}/(R\ L_z),$$

$$k_{37} = -\ C_{11}/L_r^2 + C_{31}/(2\ R\ L_z) - C_{13}/(2\ R\ L_r) + C_{33}/(4R^2),$$

$$k_{63} = -\ 2\ C_{21}/(L_r\ L_z) + C_{23}/(L_z\ R),$$

$$k_{66} = 4\ C_{22}/L_z^2,$$

$$k_{67} = 2\ C_{21}/(L_r\ L_z) + C_{23}/(R\ L_z),$$

$$k_{73} = -\ C_{11}/L_r^2 - C_{31}/(2\ R\ L_r) + C_{13}/(2\ R\ L_r) + C_{33}/(4R^2),$$

$$k_{76} = C_{12}/(L_r\ L_z) + C_{32}/(2\ R\ L_z),$$

$$k_{77} = C_{11}/L_r^2 + C_{31}/(2\ R\ L_r) + C_{13}/(2\ R\ L_r) + C_{33}/(4R^2)$$

All other elements of the stiffness matrix are zero.